# UC Santa Cruz
## UC Santa Cruz Electronic Theses and Dissertations

**Title**

Performance of Ultra-Fast Silicon Detectors at the Fermilab Test Beam Facility

**Permalink**

https://escholarship.org/uc/item/99t4h6ch

**Author**

Freeman, Patrick Moriishi

**Publication Date**

2017

Peer reviewed|Thesis/dissertation

UNIVERSITY OF CALIFORNIA
SANTA CRUZ

**PERFORMANCE OF ULTRA-FAST SILICON DETECTORS AT THE
FERMILAB TEST BEAM FACILITY**

A thesis submitted in partial satisfaction
of the requirements for the degree of

MASTER OF SCIENCE

in

PHYSICS

By

**Patrick M. Freeman**

September 2017

The Thesis of Patrick M. Freeman
is approved:

_____
Professor Hartmut F.-W. Sadrozinski, Chair


_____
Professor Michael Hance


_____
Professor Abraham Seiden


_____
Tyrus Miller
Vice Provost and Dean of Graduate Students

Performance of Ultra-Fast Silicon Detectors at the Fermilab Test Beam Facility

# Table of Contents

List of Figures

iv

List of Tables

Abstract

Performance of Ultra-Fast Silicon Detectors at the Fermilab Test Beam Facility

By Patrick M. Freeman

We report on the performance of 50μm thick Ultra-Fast Silicon Detectors (UFSDs) made by Hamamatsu Photonics (HPK) and Centre Nacional de Microelectronica (CNM) Barcelona at test beams at Fermilab National Accelerator Laboratory (FNAL). Using the precision particle tracking available at FNAL, we measured the spatial dependence of parameters including the time resolution and gain of UFSDs. We observed and documented unexpected differences in signals due to a lack of metallization on the top of sensors. We measured the widths of inactive areas in 2x2 arrays of 9mm$^2$ square pixel sensors, a limiting factor in particle detection. We also compared the timing performance of ~1mm$^2$ single diode sensors with different digitizers. We measured time resolutions near 30ps for diodes at a gain near 15 with the CAEN V1742 digitizer board and Teledyne Lecroy WavePro 725Zi.

For my family, myself, and the late Jackson Trevor Lusk. May you rest in peace.

Chapter 1: Introduction

1.1 Silicon Tracking Detectors in Particle Physics

Silicon detectors have been used in particle physics experiments for decades to track the positions of particles. In modern day implementations, such as at ATLAS at the LHC, tracks are reconstructed from information from arrays of millions of detectors. The reconstruction allows for the identification of vertices at which particles collided (or otherwise changed momentum) and in conjunction with calorimetric and other measurements, the identification of particles and potential discovery of new phenomena. In particular, the Higgs boson was discovered at the LHC in ATLAS and CMS in 2012.

Currently, the LHC is undergoing an upgrade which will increase the luminosity by a factor of 5 to 10. One predicted impact of the increased luminosity is an increase in the spatial density of interactions and therefore pileup. In the case when two events in the same bunch crossing occur at nearly the same position, without information about when the events occurred, the two events may be assigned to the same vertex. This is known as pileup. With 4-dimensional tracking, it may be possible to distinguish the two events that were piled into a single vertex, and thereby improve tracking, particle detection, and overall detector performance. Hence, as part of the ATLAS Phase-II Upgrade, a High Granularity Timing Detector (HGTD) is being constructed to provide precision timing and position tracking capabilities.

1

1.2 Working Principle of Silicon Detectors

Silicon detectors in particle physics are typically planar structures that consist of a p-doped or n-doped bulk and thin implantation of the opposite doping. In n-doped (p-doped) material, electrons (holes) are the majority of charge carriers, and group-V (group-III) elements are typically used to dope the silicon. For the purposes of this discussion, let us assume that we have a p-bulk and n-implant. The boundary between the bulk and the implantation forms a p-n junction.
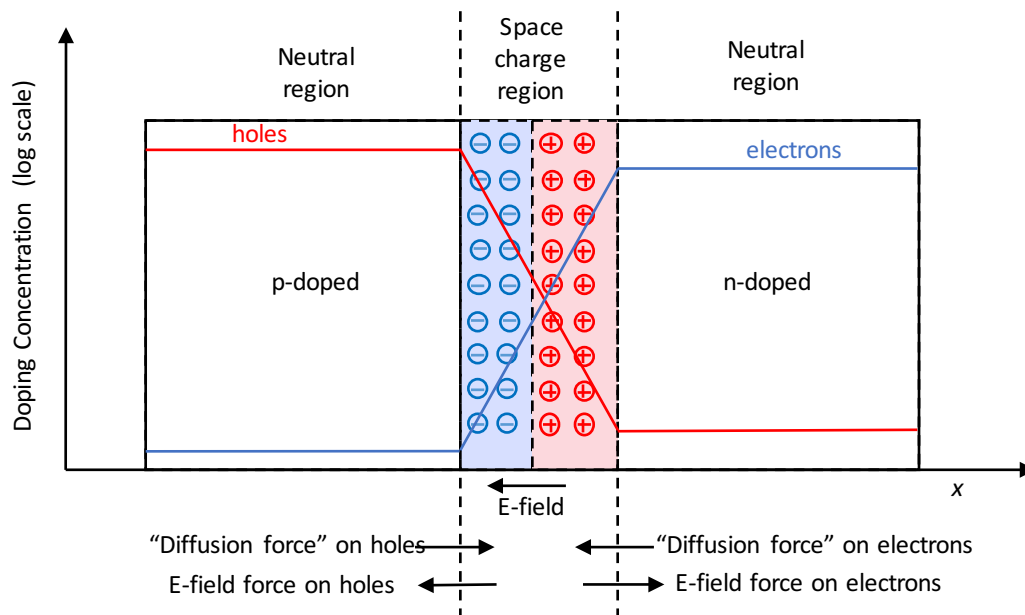


Figure 1. A p-n junction at zero bias.

At zero bias, regions near the p-n junction lose their neutrality as electrons diffuse from the n-type material towards the p-type material, and vice versa for the holes [1]. This results in an electric field pointing from n-type to p-type that counteracts the diffusion process until an equilibrium is reached. The region where

charge carriers have been removed is known as the space charge region or depletion region. A p-n junction at equilibrium is shown in Figure 1.

Silicon detectors are operated under reverse bias, that is, with the positive voltage applied to the n-type silicon. As the DC voltage is increased, the electric field increases and further expands the depletion region. Full depletion is achieved when the entire sensor has been depleted. When a particle passes through the depleted silicon, electron hole pairs will form along the path of the particle and separate and drift under the influence of the electric field. If the silicon were not depleted, there would be no field and the electron hole-pair would not drift in any particular direction and eventually recombine. The induced current resulting from drifting carriers is the signal, which is readout. The working principle of a silicon detector is illustrated in Figure 2, though this is for a 300μm thick strip detector; we discuss 50μm thick detectors in this thesis.
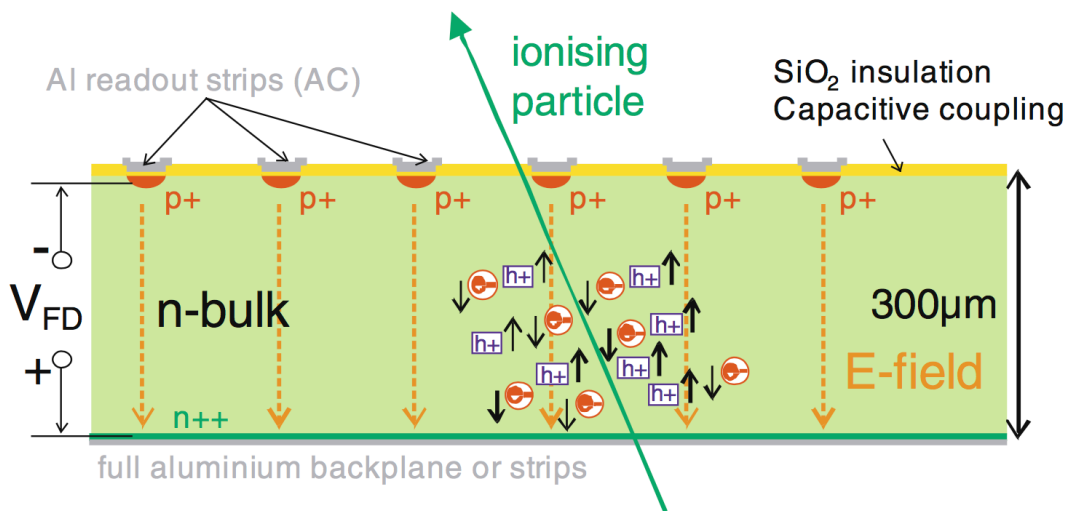
Figure 2. Working principle of a silicon detector, in this case a 300μm thick AC-coupled microstrip detector [1]. An ionizing particle passes through the detector, forming electron-hole pairs which travel to the electrode due to the E-field.

3

1.3 UFSD

Ultra-Fast Silicon Detectors are silicon detectors designed to provide 4-dimensional tracking of particles in physics experiments [2], with the ultimate goal of position resolution on the order of 10μm and timing resolution on the order of 10ps. They are being developed as an integral part of the High Granularity Timing Detector (HGTD). For HGTD, the performance goals are to have a 1mm by 1mm granularity and 30ps time resolution for each layer and a detector consisting of four layers of silicon sensors [3]. The entire new detector will be placed between the liquid argon barrel and endcap cryostats. Furthermore, silicon detectors must be radiation hard in order to operate for years in the LHC. During their potential lifetimes, sensors would receive reach fluences on the order of a few times $10^{15}$ neq/cm$^2$.

The UFSDs we studied for this thesis are known as Low Gain Avalanche Diodes (LGADs). The design of LGADs was inspired by avalanche photo diodes (APD), photodetectors with built-in gain due to an avalanche region with a high electric field. The high field accelerates carriers enough that they free more carriers, which in turn free more, resulting in an avalanche of charge carriers, and signal gain. [4]. The high field is created by the doping profile of APDs, which consists of highly doped n+ implantation, moderately doped p implantation, and p- bulk. The main parameter that sets the gain is the doping concentration in the p implant layer. LGADs differ from APDs only in that they have lower gain due to a decrease in the

4

doping of this p layer [5]. We show a schematic of the LGAD design in Figure 3, which is equally applicable to an APD.

The gain of a silicon sensor can be roughly modeled using an exponential function to compute the total number of charge carriers $N$ generated by a particle that has traveled a distance $x$ in a high field region as

$$N(x) = N_0 \, e^{\alpha x}$$

where a number of competing theories are used to compute the $\alpha$ factor as monotonically increasing function of the electric field [6, 7]. The gain is defined as the ratio of total charge carriers detected to carriers generated, $N/N_0$.
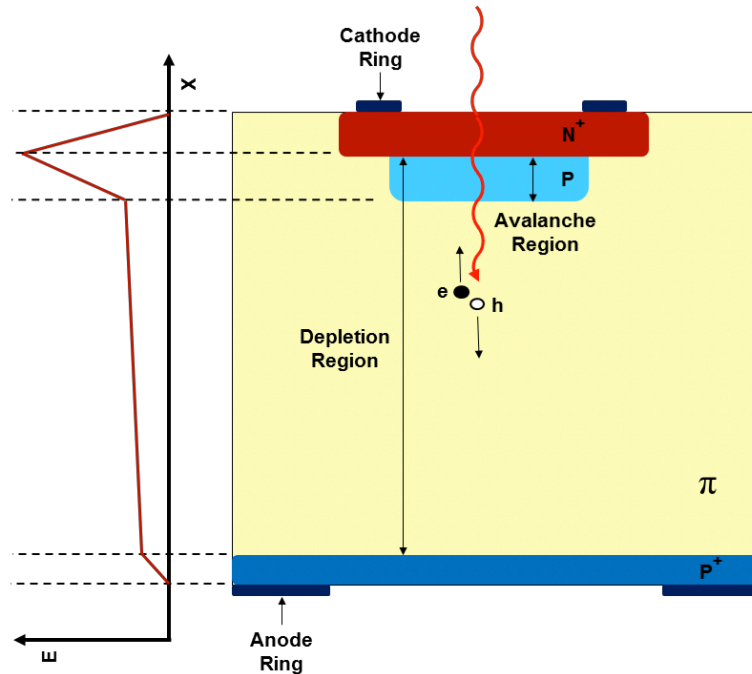


Figure 3. Schematic of an n-on-p LGAD operated under reverse bias [8]. The red line depicts a particle passing through the sensor. The electric field will be highest at the junction, as indicated by the graph on the left. This region is known as the avalanche region, where charge multiplication occurs.

In a previous study, we measured a time resolution of ~50ps at gain > 20 for

50μm  ~1mm$^2$ diode LGADs before and after irradiation [9]. The area of a sensor is

of importance since for a given thickness it is proportional to the capacitance of the

sensor, which can affect the rise time of signals and timing performance. We noticed

a strong dependence of the timing resolution on the gain of sensor, as depicted in

Figure 4. With this success, there are number of further open questions we answer to

some degree in this thesis: the uniformity of performance across the entirety of

individual pixels and diodes, the effects of different digitizers, and the performance of

irradiated sensors (though many other results on this are being published, or already

have been). We also investigate and size of inactive regions of these detectors, and

compare results for CNM and HPK. This measurement, along with the uniformity

studies, requires the high precision particle tracking capabilities at the Fermilab Test

Beam Facility [10].
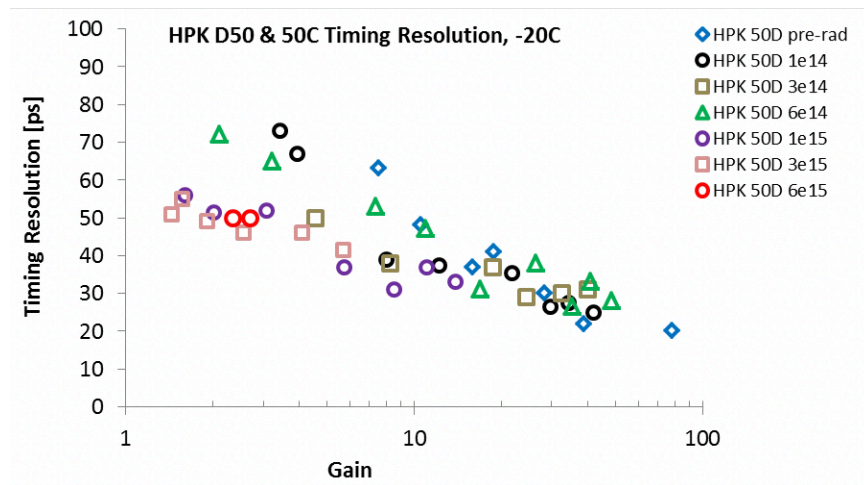


Figure 4. Time resolution vs. gain for HPK single diodes [9].

We tested 50μm thick UFSDs from production run 9088 by CNM and run ECX20840 from HPK with an active layer thickness close to 50μm. From HPK, we studied sensors of doping concentrations denoted as C, and D, with C being the lower concentration and D the highest. The manufacturer values for doping concentration of these HPK sensors are currently confidential, though measurements show that each doping concentration differs by about 4% [11]. HPK also produced type 'A' and 'B' sensors of lower doping concentration that are not subject of this thesis. From CNM we had sensors of three doping concentrations, though in this thesis we only discuss the performance of the highest two, 1.9e13 atom/cm$^2$, and 2.0e13 atom/cm$^2$, which in this thesis correspond to wafers W9 and W11, respectively [12]. The active areas of detectors varied from between .8mm$^2$ and 9mm$^2$, enabling us to see variations in global parameters such as signal rise time as a function of the capacitance.

We studied 2x2 arrays from HPK and CNM, and determined the dimensions of inactive regions and the uniformity of sensors. In particular, we noticed a lack of uniformity due to effects of metallization in an irradiated diode from CNM and non-irradiated HPK array. As one can see in Figure 5, the CNM diode W11LGA35 has a circle in the center of the diode where there is no metal on top of the silicon oxide, and the HPK arrays in Figure 6 (right) have a square of metal in the center of the array and no metal outside of this. On the other hand, the CNM array W9HG11 and HPK 50D single diode have continuous metallization that covers the entire active region. A table of sensors analyzed in this thesis is below.

7

Table 1. Table of UFSD

| Manufacturer | Sensor number | Size of gain region | Description | Readout | Fluence (neq/cm$^2$) | Tested at | Bias Voltages (V) |
|---|---|---|---|---|---|---|---|
| CNM | W9 HG11 | 3mm x 3mm | 2x2 pixel array | 4-channel UCSC board | 0 | FNAL | 140, 160, 180 |
| HPK | 50C PIX | 3mm x 3mm | 2x2 pixel array | 4-channel UCSC board | 0 | FNAL | 410, 450, 470 |
| CNM | W11 LGA35 | 1mm x 1mm | Single diode | Single Channel UCSC board | 6 E+14 | FNAL, UCSC | 400 |
| HPK | 50D | 1mm diameter | Single diode | Single Channel UCSC board | 6 E+14 | FNAL, UCSC | 600 |
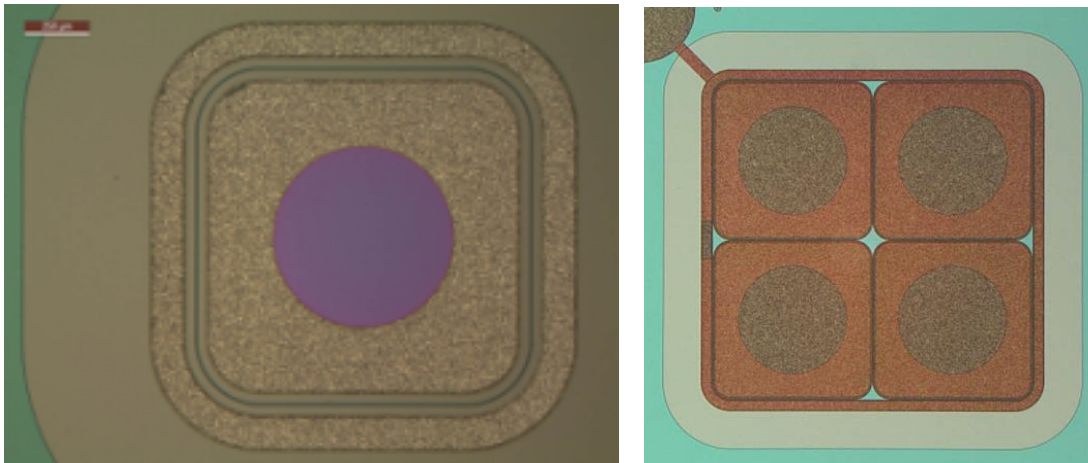


Figure 5. Photographs of CNM LGADs(left) A single diode. The purple region in the center does not have metal. (right) A 2x2 array. The circular region in the center of each pixel is just a hole in the passivation, there is still metal on top of the sensor in this region.
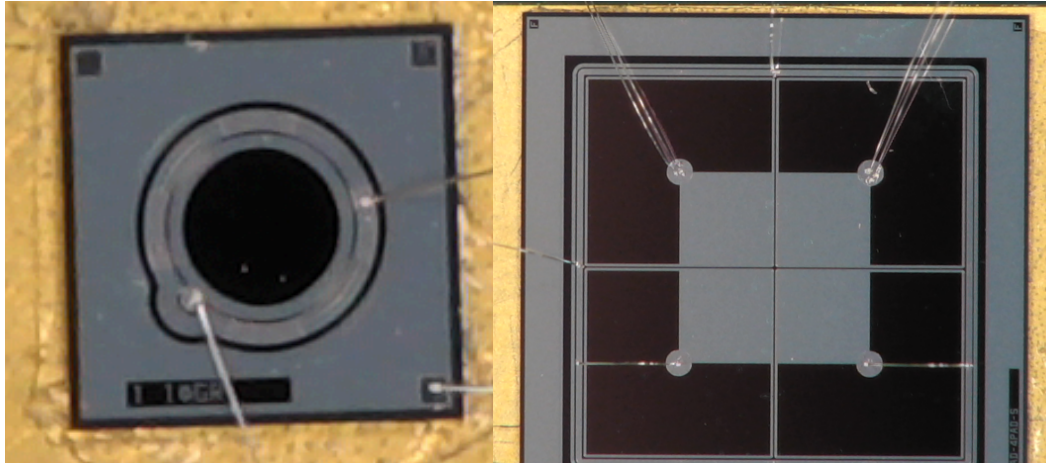
Figure 6. Photographs of HPK LGADs. (left) Photograph of an HPK 50D diode, mounted on a readout board. (right) Photograph of an HPK PIX sensor with 4 pixels each of area 9mm$^2$ mounted and wire bonded to a readout board. In this image, a two-channel board is used, so the lower two pads are shorted to the guard ring and ground, and upper two to amplification for readout.

1.4 Readout Boards
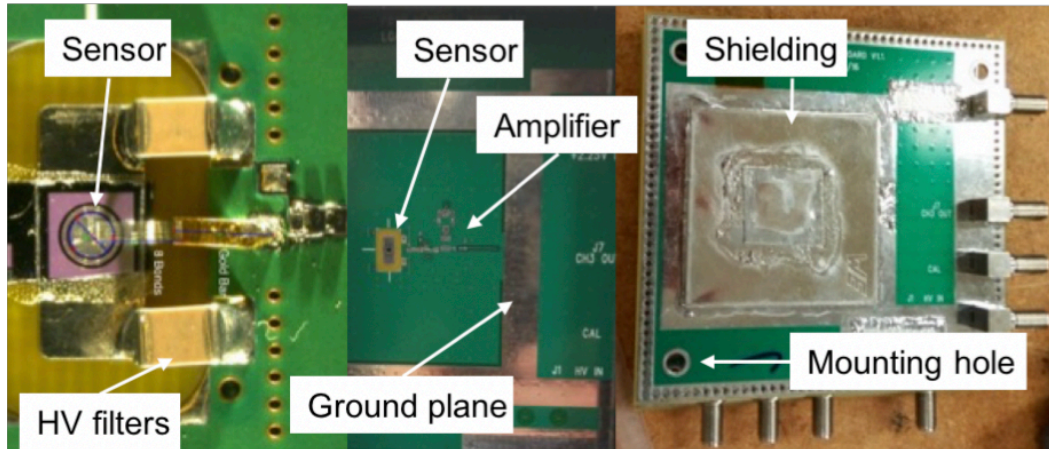


Figure 7. Single channel readout boards. (left) A mounted UFSD. (center) Bare board before shielding is attached. (right) Board with shielding.

In order to measure the current induced from energy loss of particles, SCIPP

engineers designed readout boards to amplify the signal from sensors. The single

channel boards are pictured in Figure 7. They were designed with discrete

components and have a number of features to minimize noise at high bandwidth

(~2GHz). By-pass capacitors were mounted next to the sensor to filter the high voltage. The amplifier is also mounted near the sensor to reduce the chance of additional noise being amplified. The boards include electrical shielding for the sensor and pre-amplifier as to reduce the effects of electromagnetic interference. The length of wire bonds is kept to a minimum to reduce inductance; a gold pin is soldered to the bias pad to this end.

The boards also served to align sensors. They were designed with holes near the four corners through which steel rods could be placed in order to align the boards and thereby the sensors within the telescope frame.

On the readout boards, there is a transimpedance amplifier made of discrete components, including a Si-Ge transistor. A transimpedance amplifier converts current to voltage and the gain can be characterized by the resistance of the feedback resistor. In a simple model, the transistor sets the current through the feedback resistor to be equal to the current in the detector, and the output voltage is then

$$V_{out} = I_{induced} \, R_{transimpedance}$$

and the transimpedance is simply the resistance of the feedback resistor. Then, we calculated the current and collected charge, $Q$, as

$$I = \frac{V}{R}$$

$$Q = \frac{1}{R}\int V\,dt = \frac{1}{R}\sum V_i\,\Delta t$$

where the limits of integration are defined by the beginning and end of the pulse. The last equality assumes discrete values for time and voltage, as is the case for digitized waveforms.

The amplifier transimpedance was simulated to be frequency dependent, as shown in the SPICE simulation in Figure 8. Though the simulated value for single channel board's transimpedance in simulation is 390$\Omega$, we use a value of 470$\Omega$ analysis that matches the corresponding discrete component. For single channel boards, we also used a secondary, external, amplifier, a Mini-Circuits Gali52+ with 2.0 GHz bandwidth, and gain of 20.8 dB at 1 GHz. To account for this second amplifier, we scaled the voltage by a factor of 1/10 prior to calculating the current. For 4-channel boards, a value of 10700$\Omega$ was used for the on-board three stage amplifiers; no external amplifier was necessary. Due to uncertainty of the exact frequency behavior of our signals, which include components above 700MHz, and observed variance in the behavior of amplifiers of 10% in gain, we estimate a 20% uncertainty in the scale of gain measurements.
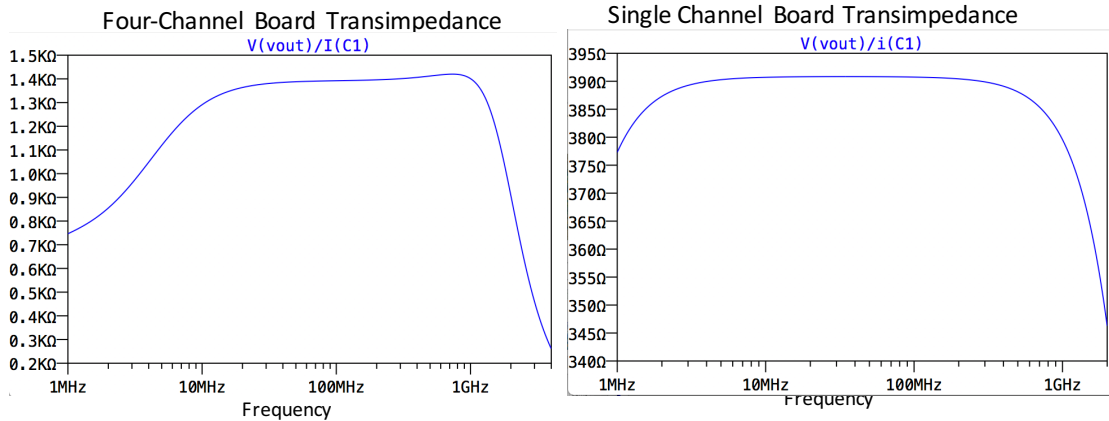
**Figure 8.** LT SPICE simulations of readout boards. made by SCIPP engineers of the transimpedance as a function of frequency in (left) 4-channel boards (right) single channel boards. For the 4-channel board, there is a commercial amplifier on the board which we treat as having gain 10, so transimpedance values are 10 times what is shown here. In (left) and (right), the gain decreases as a function of frequency. The 3dB values are ~3.3GHz in (right) and ~1.8GHz in (left).

1.5 Test Beam Facility at Fermilab

We tested detectors at the Fermilab Test Beam Facility (FBTF), which provided a beam of 120GeV pions bunched at 53MHz. We placed detectors on a motorized, remotely controlled, stage within the pixel telescope that provides position resolution better than 10μm for particles passing through the detectors under test (DUT) [10]. We estimate this position resolution in the inactive area width measurements in Chapter 2 as the sigma of the error function fits. A Photek 240 micro-channel plate photomultiplier was used as a trigger to provide a fast time stamp for particles. It was previously measured to have a time resolution of 10ps [13]. For a DUT with a time resolution of 30ps, the combined time resolution would be $\sqrt{30^2 + 10^2} = 31.7$ ps. This is a difference of 6%, and hence we neglect the contribution of the MCP to the time resolution. The aluminum support structures for

DUT are equipped with Peltier cooling elements that enabling cooling to -20° C.

Additionally, the entire stage for DUT could be remotely controlled to move

vertically and horizontally to align sensors with the beam. Track reconstruction was

performed using the Monicelli software package developed specifically for the test

beam application [10].
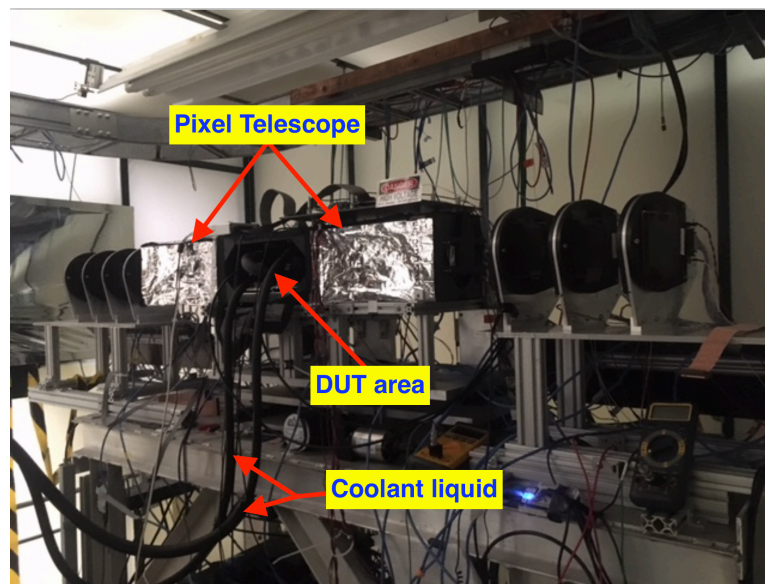


Figure 9. The experimental enclosure at FNAL. Detectors were placed in ESD shielded boxes in the DUT area between the ends of the pixel telescope. Coolant is provided to the detectors and Peltiers via the labeled pipes.
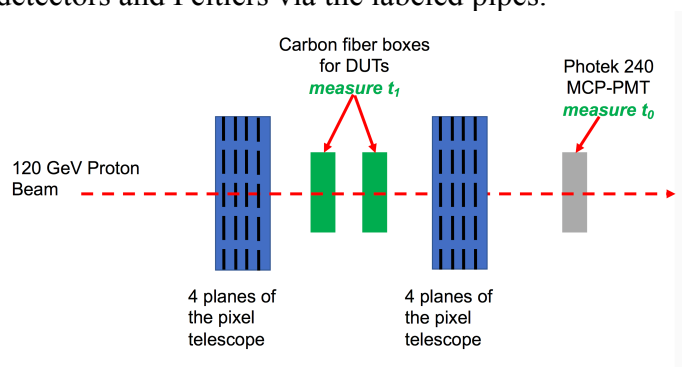


Figure 10. Schematic of the test beam setup[14].

For acquisition of the timing data we used a CAEN V1742 digitizer, which records digitized waveforms at a sampling rate of 5GS/s and 500MHz bandwidth. Its optimal time resolution was measured to be ~4ps in [15], and is neglected in timing studies. In Chapter 4, we show analysis of waveform data acquired with a beta source at UCSC. In this case, for data acquisition we used a Teledyne Lecroy WavePro 725Zi oscilloscope with a sampling rate of 40GS/s and 2.5GHz bandwidth. The data acquisition at UCSC is described in detail in [16], [17].

1.6 Analysis methodology

Digitized waveforms are analyzed to extract sensor parameters such as the gain, time resolution, and rise time, as in [17]. For the CAEN V1742, these data come in the form of a discrete time and ADC counts vectors for each event, with 4,096 ADC counts corresponding to 1 volt. An example of a waveform is plotted in Figure 11.
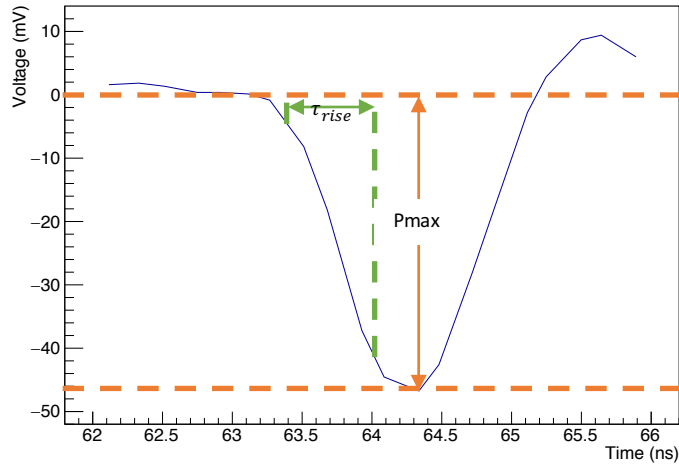


Figure 11. A digitized waveform, converted from ADC counts to voltage. The rise time, $\tau_{rise}$, and pulse maximum, Pmax, measurements, are illustrated.

All events are corrected for any DC voltage offset by averaging the voltage in the region prior to the pulse, and then subtracting this value. The noise RMS is calculated as the standard deviation of the voltage in this region, and a Gaussian is fit to the distribution of RMS measurements from many events. We report the mean of the Gaussian as the noise RMS of the sensor.

After the DC offset correction, all pulses first shifted in time such that 50% of the trigger pulse height occurs at t=0, thus ensuring all events should occur within the same window of time. This correction also accounts for the time walk of the trigger, which can be quite drastic, as illustrated in Figure 12.
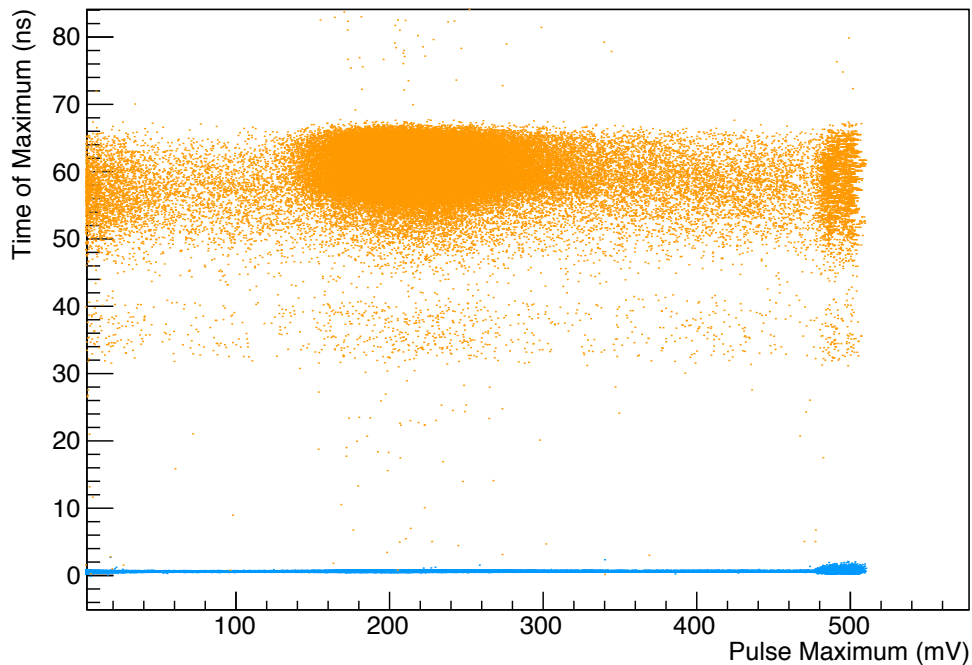


Figure 12. Time of maximum vs. pulse maximum of the trigger for corrected (blue) and uncorrected (orange) events. The correction eliminates a time walk in the trigger on the order of nanoseconds. The width of the corrected (blue) distribution is ~300ps.

Then real events, that is, signals corresponding to particles passing through the DUT, are defined as those which pass a number of cuts. One cut is that time of the pulse maximum in the DUT must be within ~300ps of its mean. That is, the delay between the DUT and trigger is consistent, as should be the time of flight for particles. Another is the pulse height must be above the noise floor, defined as five times the noise RMS, and below the saturation level of the readout electronics. These cuts are illustrated in Figure 13. We also make a cut on the time of the maximum in the trigger sensor to avoid pileup events or trigger pulses that have long rise times. In the case of arrays or uniformity studies additional cuts may be made, for example on the position of events or on 'cross-talk' events where there is signal in multiple pixels of an array.
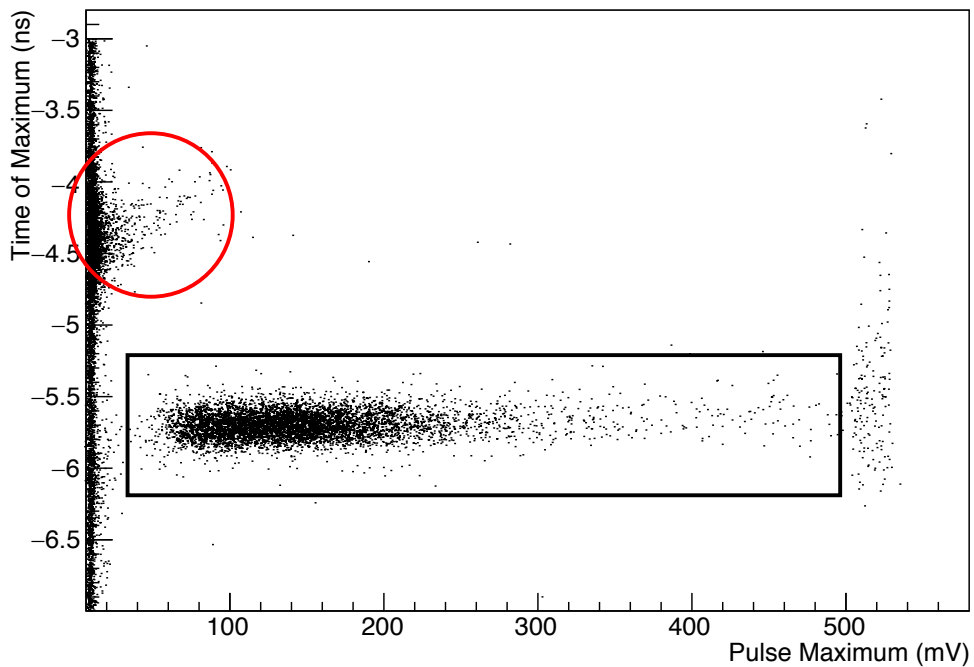
Figure 13. Time of maximum versus pulse maximum for a DUT. The cuts on the pulse maximum and time of the maximum result in the signals in the black box being tagged as events. Events in the red circle are on oscillation specific to the readout board.

We calculate time resolution as the sigma of the Gaussian fit to the distribution of differences in timestamps between the trigger and DUT signals. We define the time stamps as the time at which a specified percentage of the pulse height is crossed on the pulses leading edge. We denote this percentage as the constant fraction discriminator percentage (CFD%), due to the algorithms inspiration. In certain studies, the CFD% is varied to yield an array of time resolution results.

We calculate the gain of sensors by calculating the collected charge as the pulse area divided by the effective transimpedance of the readout electronics as

described in section 1.2. To calibrate the charge, we divide by the predicted collected

charge for a minimum ionizing particle (MIP) passing through a $50\mu$m silicon sensor,

calculated based on [18]. For an unirradiated $50\mu$m sensor, the value is 0.51fC. To

calculate the gain of the entire sensor, we fit a Landau distribution to the distribution

of gain values and report the most probable values.

We calculate the pulse maximum as the maximum voltage value and rise time

as the time between 10% and 90% of the pulse height. The time and voltage measured

by these calculations are illustrated in Figure 11. To characterize the detector, we fit

the pulse maximum and rise time distributions with Landau and Gaussian

distributions, respectively.

Chapter 2: Array Inactive Region Width Estimation

An important characteristic of pixel arrays is the width of the inactive region, the area where particles that pass through the sensor will not be detected. The larger this area, the lower the detector efficiency.  However, placing the pixels closer together is a technological challenge. In this chapter, we discuss the importance of the fill factor in particle detection, and show measurements of the width of the dead regions.

2.1 Fill Factor
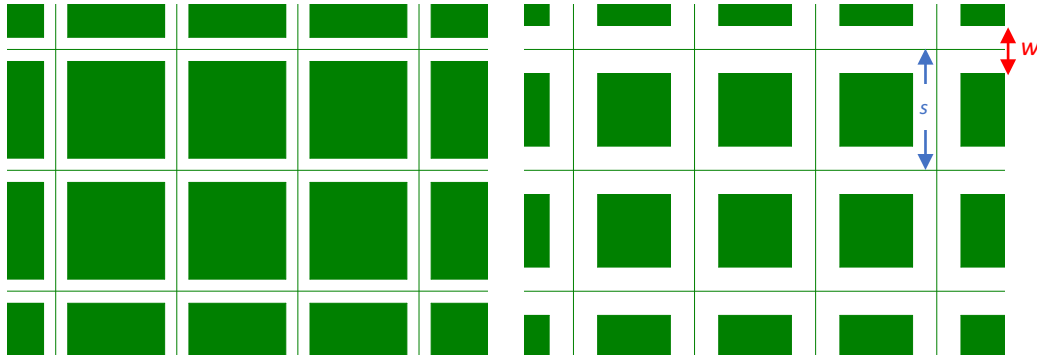


Figure 14. Schematic of arrays of pixels with $s$ = 1mm pitch. The active area is the filled, green, center of each square within the pixel. In (left) the width is $w$ = 200µm, in (right) $w$ = 400µm.

The fill factor of a detector is defined as the ratio of the active area to the total area. In Figure 14., this corresponds to the ratio of the area of filled green squares to the total area. We can calculate the fill factor as:

*Fill factor = Active Area/Total Area = (Total Area – Inactive Area)/(Total Area)*

For arrays of square pixel detectors with a set pitch, the fill factor, *F,* as a function of the pixel size, *s*, and width *w*, of the inactive regions is

$$F = [(s - w) / (s)]^2$$

which will be approximately linear when the width of the inactive region is much smaller than the size of the pixels. For 1mm pixels with a 100μm width this gives a fill factor of .81/1 = 81%. In Figure 14 (left) the 200μm width results in a smaller fill factor of only 64%, and in (right) the 400μm width results in a 36% fill factor.

If we assume a series of planar detectors with same fill factor and that the probability of a particle being detected in one layer is independent of the probability of detection others (or equivalently, that the active regions are randomly distributed), then we can model the probability of detection using a binomial distribution. Then, for $n$ layers, the probability, $P(k)$, of detecting the particle in exactly $k$ layers is given by

$$P(k) = \binom{n}{k} F^k (1 - F)^{n-k}$$

where

$$\frac{n!}{k! \, (n - k \, )!}$$

A caveat here is that in a real experiment there is likely dependence between the layers based on their relative positions of the pixels and particle track trajectories. For 4 planar detectors – as is the current proposed designed of HGTD - with a given fill factor, we can calculate the probability that a particle will travel through the active regions of least three of four layers to be

$$P(3 \text{ or } 4) = P(4) + P(3) = 4 * F^3 (1\text{-}F) + F^4$$

and obtain the detection probability as a function of the width of the inactive region and pixel size. We show a plot of the fill factors and probability of detection in a four-

layer detector of 3mm$^2$ and 1mm$^2$ pixels as a function of the width in Figure 15. For

smaller pixels, which are preferable for fast timing due to their smaller capacitance,

and provide superior spatial resolution, the fill factor quickly decreases as the width

of the inactive region becomes greater. Hence, to maximize detector efficiency for

given timing and spatial resolution constraints, it is desirable to minimize the width of

the inactive regions. Equivalently, for a given efficiency, the pixel size is limited by

this width.
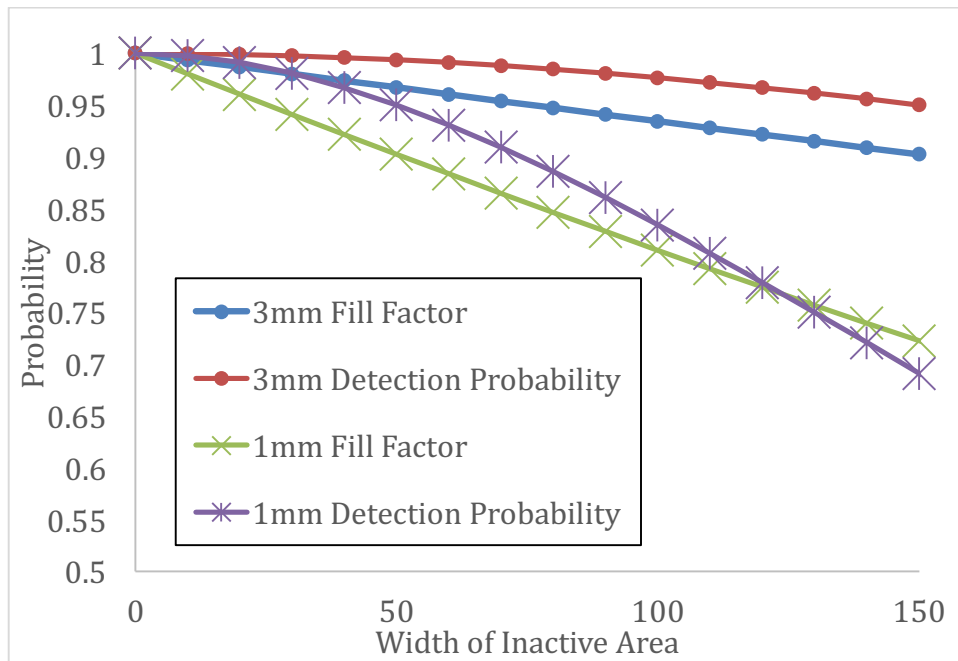


Figure 15. Fill factor and probability of hitting the active region in at least 3 of 4
planes, here called the 'detection probability.' Results for 3mm and 1mm pixels are
plotted.

## 2.2 Width measurements

### 2.2.1 Predicted dead areas

Using the position measurements provided by the pixel telescope, we were

able to measure the inactive regions and roughly confirm optical measurements of

HPK sensors and CNM schematics, which were 107μm and 63μm respectively and depicted in Figure 16.  The width for the CNM array was determined from the schematic. A 15 μm 'overhang' and 33μm region between pads sum to a 63μm dead area. For the HPK array, the width was measured under a microscope and the corresponding line is labeled as '5' in the figure. Here, we cannot be sure exactly where the gain implantation ends.
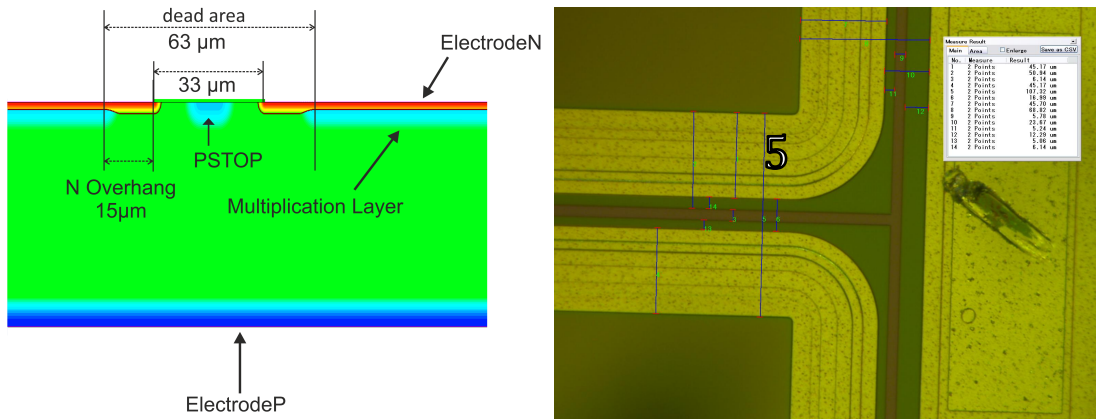


Figure 16. Estimation of widths of inactive regions. (left) Schematic of the region between pads in CNM arrays [12]. (right) Measurement of the region between pads in an HPK array made under a microscope.

2.2.2 Methodology

To measure the width of the inactive area between pads of 2x2 silicon arrays, we fit error functions to distributions of the positions of events (in a single direction at a time). Due to the limited number of data points, fits had to be made to projections along individual axes (as opposed to a two-dimensional fit of the pad or border).  In addition to the requirements for events described in Section 1.6, we made cuts to exclude charge sharing events and potential oscillations or cross-talk events. This was done with a cut that no two channels could have pulse heights above the noise floor.

We also excluded events that were near or beyond the edge of the sensor in the

direction opposite to a given profile.  A plot of the x-y positions of these good events

in the DUT is shown in Figure 17.

Due to smaller data yields than predicted, for the purposes of measuring the

dead regions runs with multiple bias voltage settings were combined. Specifically, the

CNM array is at biases of 140V, 160V, and 180V, and HPK at 410V, 450V, and

470V.
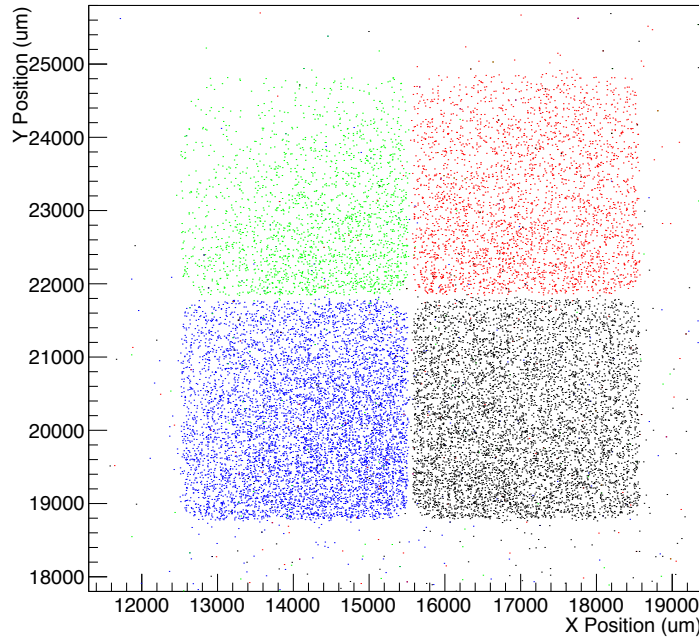


Figure 17. Positions of good events in arrays. Colors correspond to events in a given
pixel, and the x-y values have been rotated to remove skew. For the HPK sensor
(bottom), the inactive regions were not exactly perpendicular, suggesting the sensors
were also slightly askew about the x and y axes. This was actually observable on site,
as the boards did not fit flush into the cold boxes and had to be secured with Kapton
tape. The events of the CNM sensor are plotted in (top).
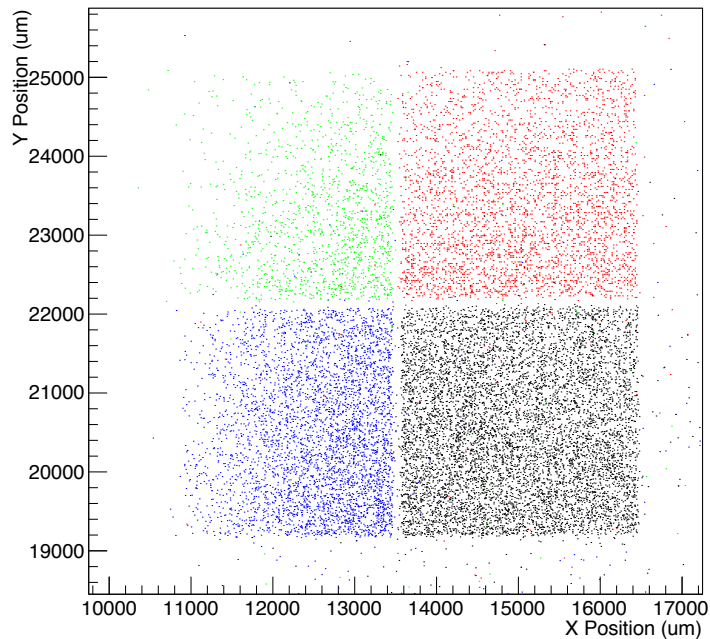
Figure 17 (bottom).

In Figure 17, a portion of events were incorrectly tracked. Some events were tracked to other pads or outside of the detector entirely, despite having a good pulse from a specific pad. Some of these missed tracks may be due to multiple scattering or pileup. However, it should be noted that the limits for pileup are strict due the requirement that the time difference between the event in the trigger and DUT be within ~1 nanosecond window. Hence, if there is a second particle, it must pass through the detector at essentially the same time. Furthermore, if the second particle went through a different pad, presumably there would be a second signal and the event would have not passed the cross-talk cut. On the other hand, we notice that there are many more background events on the side of sensor near the beam in Figure 18, suggesting that these missed tracks are related to real particles, and are not a

24

random, uncorrelated, background. In any case, we attribute particles tracked to the

dead area between pads to missed tracking, either from pileup, multiple scattering, or

the telescope's precision.
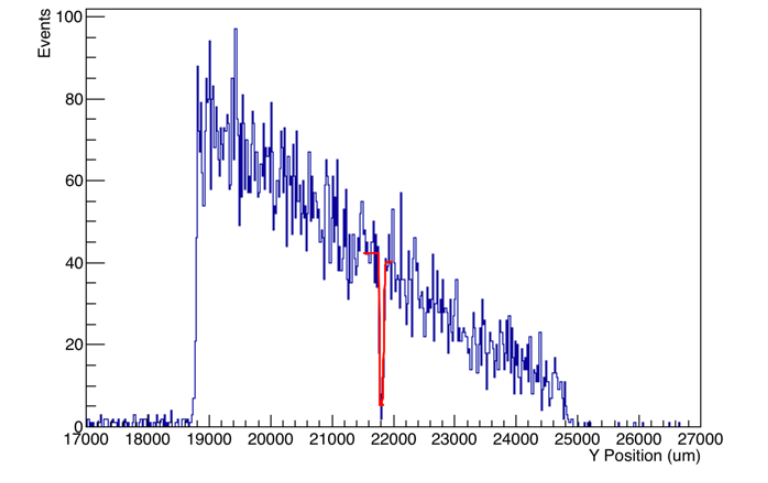


Figure 18. Profile of events in the y-direction. There are many more events near the
bottom of the sensor, and correspondingly, many more missed tracks below the
sensor than above it. The red lines are an error function fits.

In Figure 19, we plot the occupancy of the HPK array. Here it is worth noting

that we actually did not align the beam properly, but it appears that we positioned the

DUT slightly above it. This results in a bias in the occupancy and poor statistics in the

upper two pads. For this reason, results from the upper two pads are omitted in

several instances.
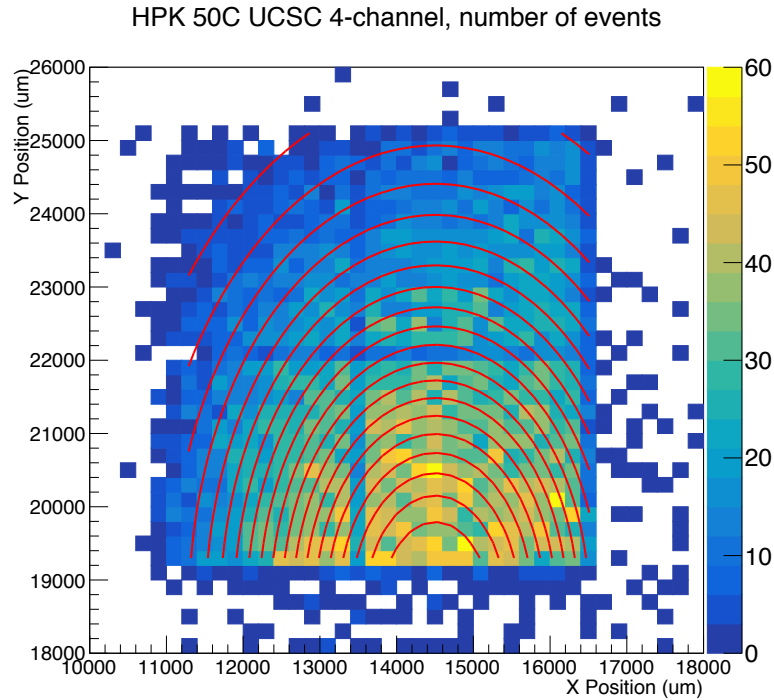
Figure 19. Occupancy profile of HPK 50C PIX at several bias voltages mounted on a UCSC 4-channel board from the FNAL test beam. A 2-dimensional Gaussian fit is shown in red. The mean is not within the detector bounds, but about 700 microns below. The sigma are measured to be 2.3mm and 3.3mm in the x and y-directions, respectively. It appears the beam was best aligned with the lower right pad. Bins are 200μm wide.

2.2.3 Results

In Figure 20, we show the error function fits to the distributions of the number of events along the horizontal and vertical directions. Each side of the detectors, corresponding to two pixels, is fit separately with an error function. The background events, which were excluded from the fits, are also plotted. Events near the gap in the active region could not be excluded, though presumably they may also be part of the background due to poor tracking, multiple scattering, or pileup, as discussed previously. We determine the edges of the inactive areas as the x-value at 50% of the

maximum of the fit. From this, we measure the widths of the inactive areas for the for

the HPK sensor be 101±7μm in the x-direction, 124±7μm in the y-direction, and

111±5μm on average. In the CNM sensor, we measure 71±5μm for the x-direction,

74μm ±6μm in the y-direction, and 72±4μm on average. We calculated the

uncertainties using the errors on the x-value at 50% of the error function fit that are

provided by ROOT's log-likelihood fitting algorithm, combining these in quadrature

to get the error in each direction, and performing a weighted average of the x and y

directions. The results of the inactive region spatial measurements are summarized in

Table 2.
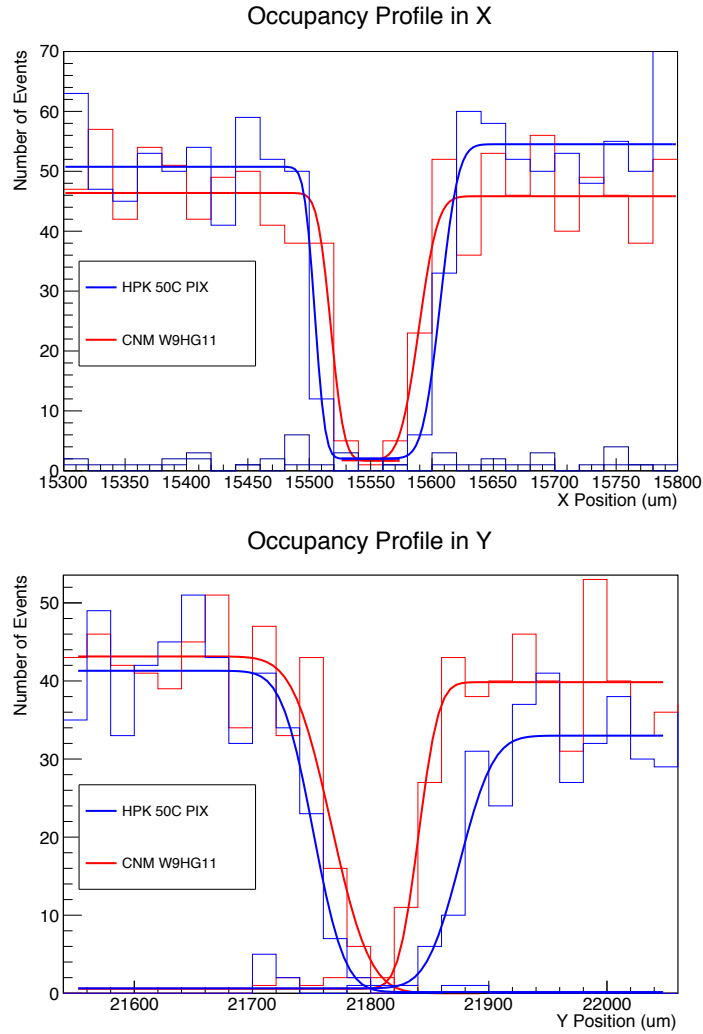
Figure 20. Occupancy profiles and error function fits to measure the width of the inactive region. Bins are 20μm wide.

Table 2. Estimates of positions of edges of gain regions. All measurements are in μm.

| Manufacturer | x1 | x1 error | x1 sigma | x2 | x2 error | x2 sigma | x width | x width error |
|---|---|---|---|---|---|---|---|---|
| CNM | 15517.5 | 3.5 | 22.8 | 15588.8 | 3.4 | 31.8 | 71.3 | 4.8 |
| HPK | 15605.8 | 2.9 | 27.0 | 15504.9 | 6.1 | 13.6 | 100.9 | 6.7 |
| | y1 | y1 error | y1sigma | y2 | y2 error | y2 sigma | y width | y error |
| CNM | 21766.8 | 4.4 | 51.3 | 21840.5 | 4.0 | 26.8 | 73.7 | 5.9 |
| HPK | 21751.4 | 5.2 | 42.0 | 21875.5 | 5.7 | 44.8 | 124.1 | 7.7 |

For the resulting widths of 111μm and 71μm, we plot the fill factors and detection probabilities in Figure 21. In order to use smaller pixels efficiently, a smaller inactive region is necessary. For 1mm pixels, a 111μm width results in 2.1 times as many particles not being detected as a 71μm width. We also note that the sigma values for fits are larger than the telescopes claimed prevision of 10μm, suggesting that it may in fact be less precise.
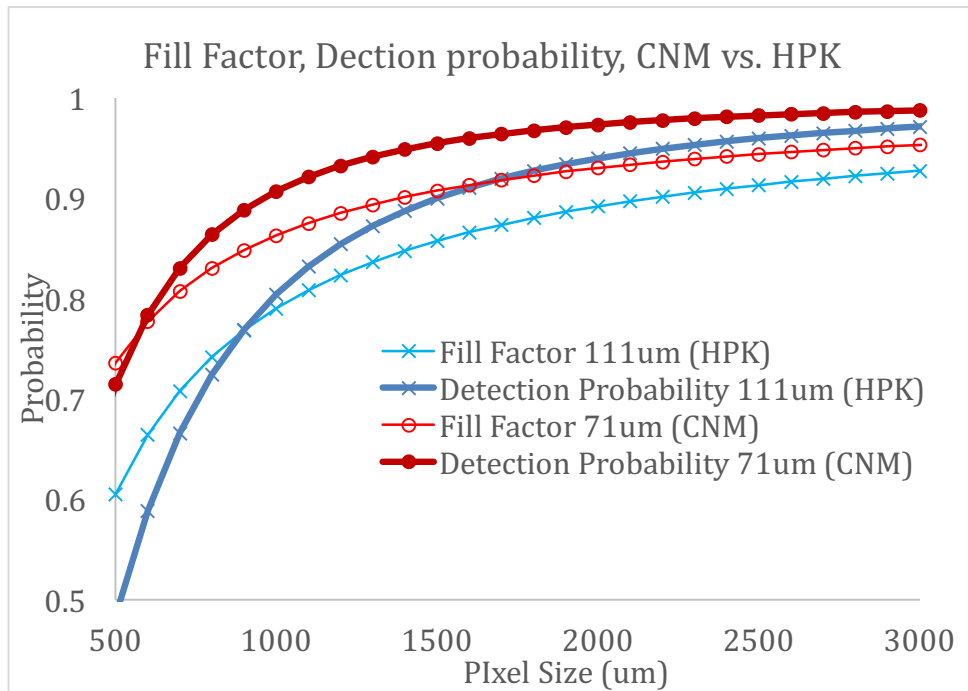


Figure 21. Fill factors and detection probabilities for the measured widths of the inactive regions in CNM and HPK arrays.

Chapter 3: Spatial uniformity of LGAD response and effects of metallization on sensors

A few of our sensors featured holes or gaps in the layer of metallization on top of sensors for the purpose of doing laser studies, as light cannot effectively penetrate the metal. In our analysis, we noticed that in these regions without metallization, the detectors performed differently, particularly for irradiated sensors. While ultimately UFSD sensors will be designed with metal on the topside, it is important to understand anomalous effects and how they pertain to the performance of sensors, and how metallization may affect the results of studies on prototype sensors (as is the subject of this thesis).

3.1 CNM diode – W11 LGA35 6e14 neq/cm$^2$

3.1.1 Sensor geometry

We studied a single irradiated CNM diode W11LGA35 irradiated to a fluence of 6e14 neq/cm$^2$, with a UCSC single channel board for readout. Due to the irradiation, the sensor current at room temperature is increased. In order to maintain a leakage current below a power supply compliance, which was set at 5uA, the sensor was cooled to -20C.
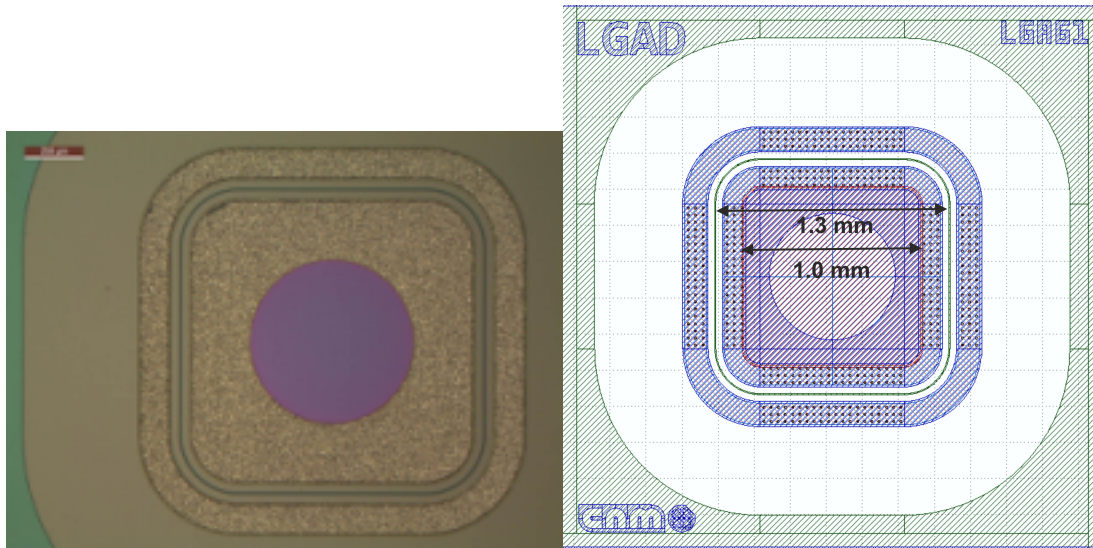
Figure 22. Photograph (left) and GDSII mask (right) of a CNM single diode. In a) the purple region in the center of the diode does not have metal, whereas the surrounding region does. In b) the gain region of the sensor is outlined in red, and measured to have a width of 1mm. The entire active region is 1.3mm wide, but the 150μm near the perimeter of the sensor does not have the p++ implant that creates the gain effect [12].

As can be seen in Figure 22, the center of the CNM diodes does not have a layer of metal on top of the silicon oxide, whereas the perimeter region is covered in metal. In Figure 22 (left) we show a two-dimensional profile of the average pulse height in millivolts as measured at the FNAL test beam. The center of the sensor, which corresponds to the region without metal, was measured on average to have significantly lower pulse heights than the perimeter region where there is metal. As illustrated in the pulse height profile in Figure 23 (left), this difference appears to be roughly a factor of two in pulse height. In Figure 23 (right) is a plot of the occupancy profile of the of the sensor. Here, the sensor has a square active area of approximate dimensions 1mm by 1mm.

31
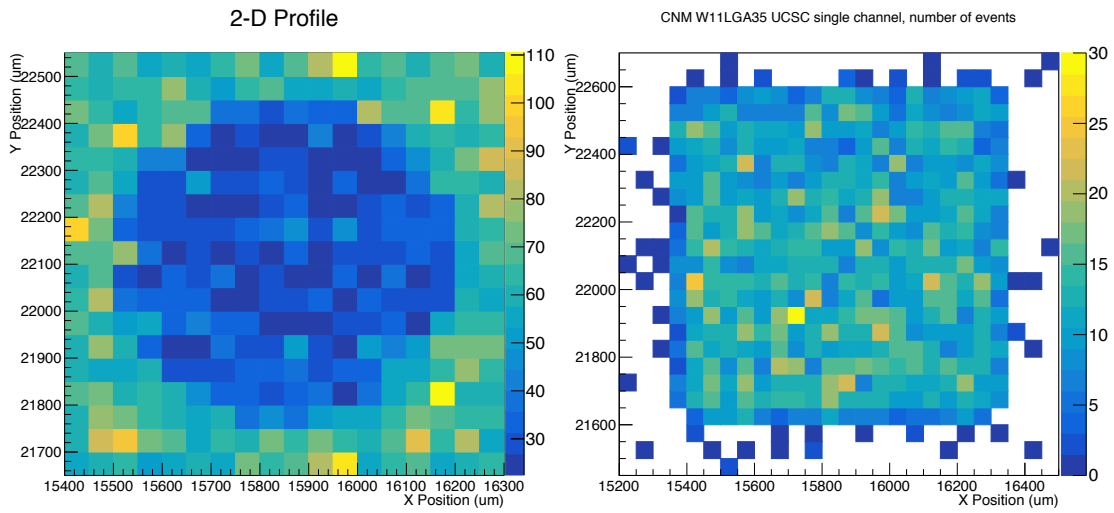
Figure 23. Two-dimensional profiles of CNM W11LGA35 6e14neq/cm$^2$, with bias voltage of -400V. (left) Pulse amplitude profile of the pulse maximum. (right) The occupancy profile. Bins are 50μm squares in both plots.

For the sake of comparison, we also include a pulse maximum profile of the single diode HPK 50D irradiated to 6e14 neq/cm$^2$. The active area of the sensor is circular with a radius of 1mm, and the entire surface of the gain region is covered in metal. Hence, we expected that the pulse height profile was uniform, which is confirmed in Figure 24. While there are some outliers with especially high average pulse heights, particularly near the edges of the sensor, we presume this to be due to

lower statistics and the Landau distribution of energy deposited in silicon.
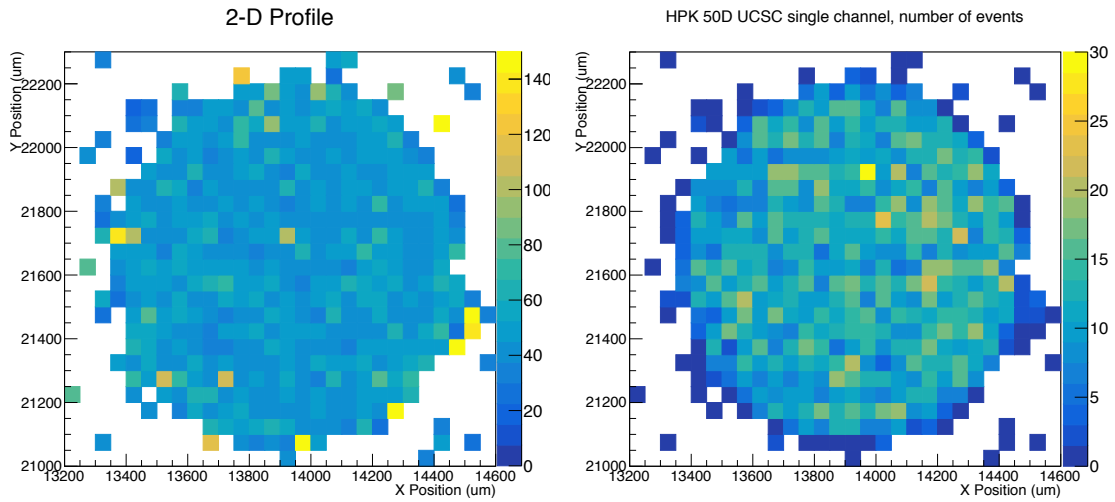


Figure 24. Two-dimensional profiles of HPK 50D 6e14 neq/cm$^2$ biased at -600V. (left) Pulse maximum profile. The color scale is truncated at 150mV. (right) Occupancy of HPK 50D 6e14neq/cm$^2$

In order to confirm the shape and approximate size of the region we have thus far referred to as non-metallized, as well as the geometry of the gain and inactive areas, we compared the pulse maximum and occupancy profiles to GDSII masks and images of the CNM single diodes. In Figure 23 (right), the size of the gain region is 1mm by 1mm. In Figure 23(left) we superimposed images of the GDSII mask of the sensor and the pulse maximum profile. Here the circular region on the profile matches that of the other two images, confirming our suspicion that the lack of uniformity coincides with the geometry of the metal. The entire size of this selection of the profile is 900μm by 900μm, and thus should fill most of the gain region of the sensor which is designed to be 1mm by 1mm; it is the region with the red outline in Figure 25 (top). In Figure 25 (bottom) we show the profile and an image of a CNM diode.

33

The profile scale is matched to the photograph scale, and the GDSII mask scaled to

matched the photograph, thus guaranteeing an approximately equal scaling of all 3.

The 900μm by 900μm region was selected since the lower statistics beyond this

region result in erratic measurements of the average pulse maximum.
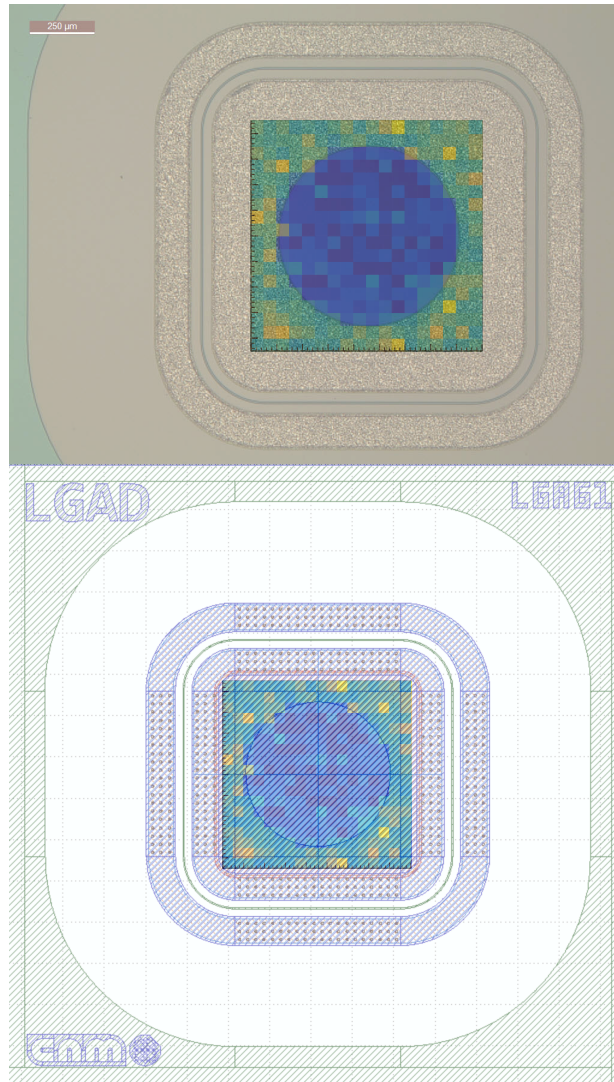


Figure 25. Superimposed images of a CNM single diode pulse maximum profile and
(top) photograph and (bottom) GDSII mask.

By making lower cuts such that the pulse height is between 25mV and 65mV,

we select only the low gain events. These are limited to the non-metallized region and

the perimeter. The occupancy profile resulting from these events is shown in Figure 26. Due to the pulse height of these events being so low, we could not select many of them without also selecting noise events, even with the requirement that events are in time. Hence, the high gain region appears sparsely populated in Figure 26, and there are not many events overall.
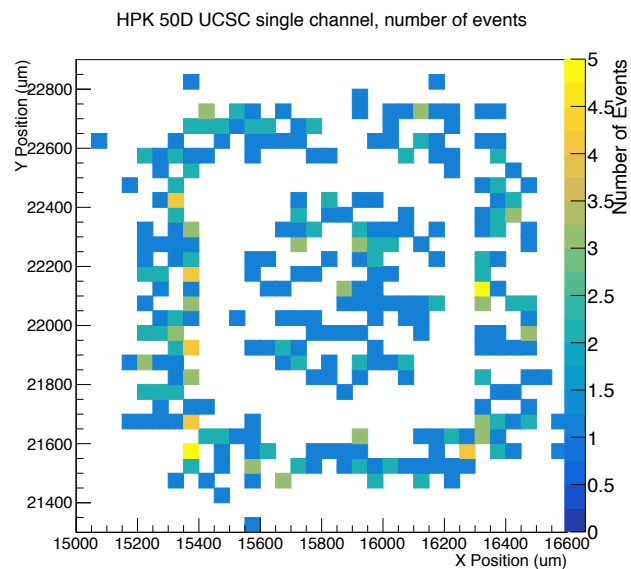


Figure 26. Occupancy profile of low gain events in CNMW11LGA35.

As with the gain region, we superimposed the images of the low gain occupancy profile with the GDSII mask and photograph of the sensor, shown in Figure 27. Again, these roughly confirm that the CNM diodes match their proposed geometry.
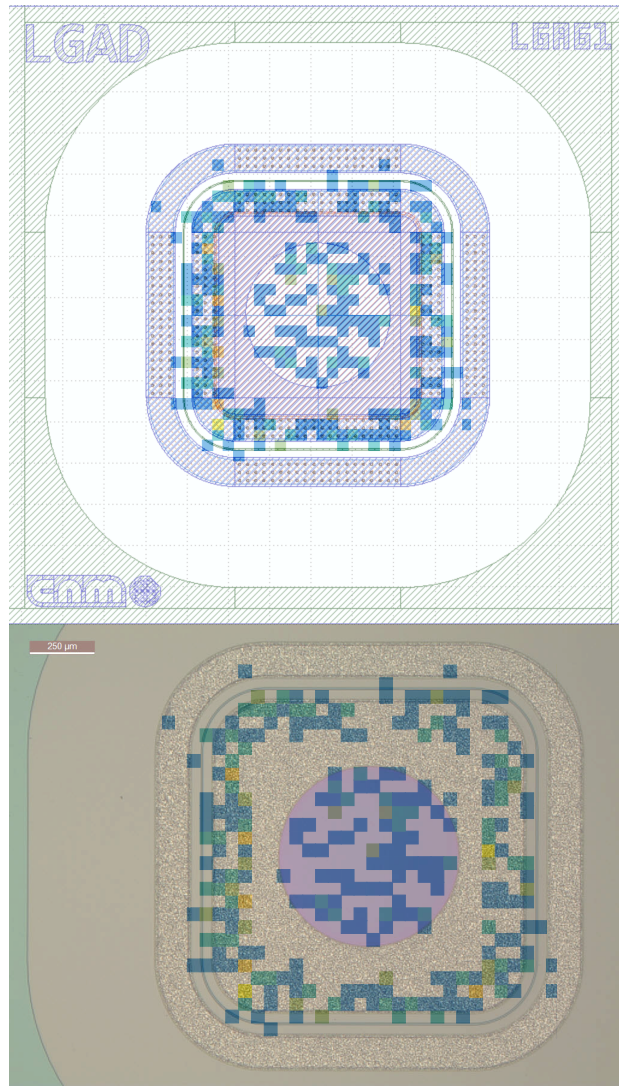
Figure 27. Superimposed images of CNM diode low gain region. (Top) Superimposed images of the low gain occupancy profile and GDSII mask for CNM W11 LGA35. (Bottom) Superimposed images of the low gain occupancy profile and photograph of a diode.

## 3.1.2 Pulse heights

We analyzed the two regions, metallized and non-metallized, of the diode

separately. To define the interior and exterior regions, they are separated by an

annulus of inner radius 350μm and outer radius 450μm, approximately centered on

the detector. The excluded region is between the two concentric circles in Figure 28 (left). In Figure 28 (right), we have plotted the pulse maximum distributions for the two regions, confirming the approximate results of the pulse max profile. The Landau fit to the distribution from the pulses in the metallized region yields a most probable value of 52mV, while fit to the maxima from the central region has a most probable value of 22mV. The ratio between the two is thus 2.4. The distribution for the entire sensor is also included in black, and has slightly more events due to the exclusion of events near the boundary of the metal and the center of the detector.
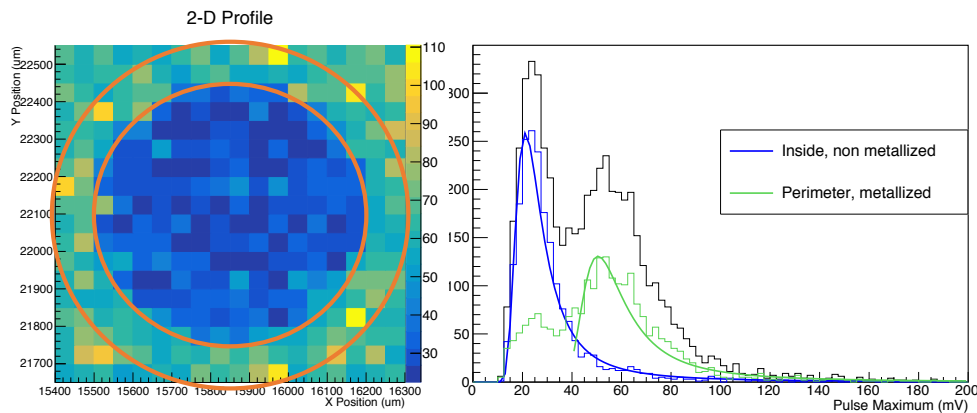


Figure 28. Pulse maximum distributions for CNMW11 LGA35 6e14neq/cm$^2$ biased at -400V (right). (left) The pulse maximum profile from Figure 23, but with concentric rings to illustrate the cuts to get the plot on the right.

3.1.3 Time delay
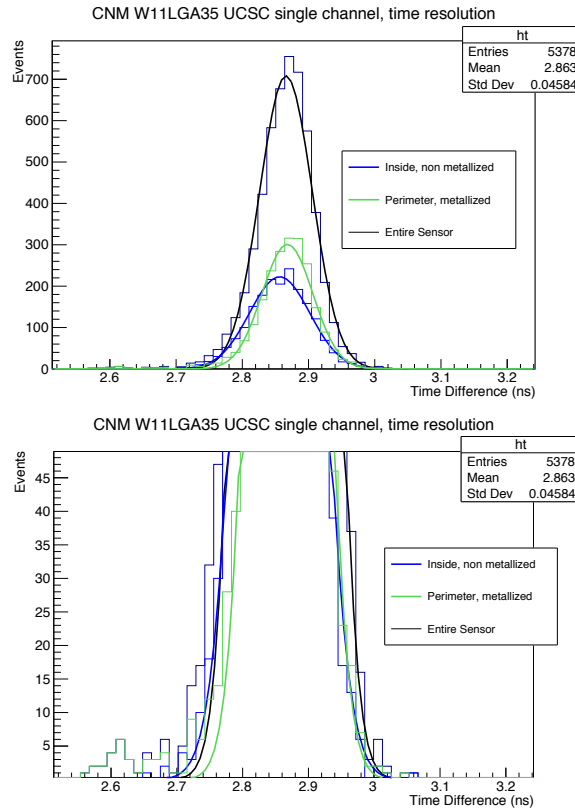
Figure 29. Distribution of time differences, CNM W11LGA35for 6e14neq/cm$^2$ biased at -400V. Differences are at 50% of pulse maximum, and fits are Gaussian. (bottom) The same distribution as (top), but with the y-axis rescaled to show a small number of events in the metallized region that arrive approximately 20ps prior to the mean of the Gaussian. There are not a comparable number of these early events from the non-metallized region.

In Figure 29 (top), we plot the distribution of time differences at 50% of pulse height and Gaussian fits to these distributions, from which we extract the time resolution as the Gaussian of the sigma. The timing resolution is the Gaussian of the fit- for metallized, non-metallized, and the entire active areas, we have resolutions of 38ps, 46ps, and 40ps respectively. Though we vary the CFD% to optimize results later in this section, Figure 29 (top) shows that mean of the Gaussian fit is greater for the pulses in the perimeter region, implying that the time of 50% of the pulse

38

maximum occurred slightly later. The delay between the two Gaussians is 12ps. Additionally, we noticed a small number of pulses from the metallized region, approximately 1% of events, with small time differences. These pulses correspond to the events to the left of the Gaussian distribution in Figure 29 (bottom).

We investigated the nature of this delay, specifically if it was due to the pulse being translated in time or if the pulse shape was significantly different, causing the timestamp to shift. To do this, we looked at normalized average pulses from the metallized and non-metallized regions. In Figure 30 (top), we do not correct the time of two pulses relative to each other, but instead the trigger, in Figure 30 (bottom)we have aligned them at 10% of the pulse height. In (top) it is apparent that the non-metallized pulse is earlier in time, but in (bottom) also that the rise time is slower. However, these differences are so small that they may arise from statistical fluctuations (as we confirmed with Gaussian fits to the rise time), and we will not conclude that the rise time is faster in either case, but simply claim that there is an indication it may be faster in the metallized region.

However, these early pulses in the non-metallized region is opposite from results presented later in which we observed late pulses in the non-metalized region away from the center of HPK unirradiated arrays. Furthermore, we do not propose a mechanism for the delay in pulses, and must describe behavior as an anomaly for the time being.
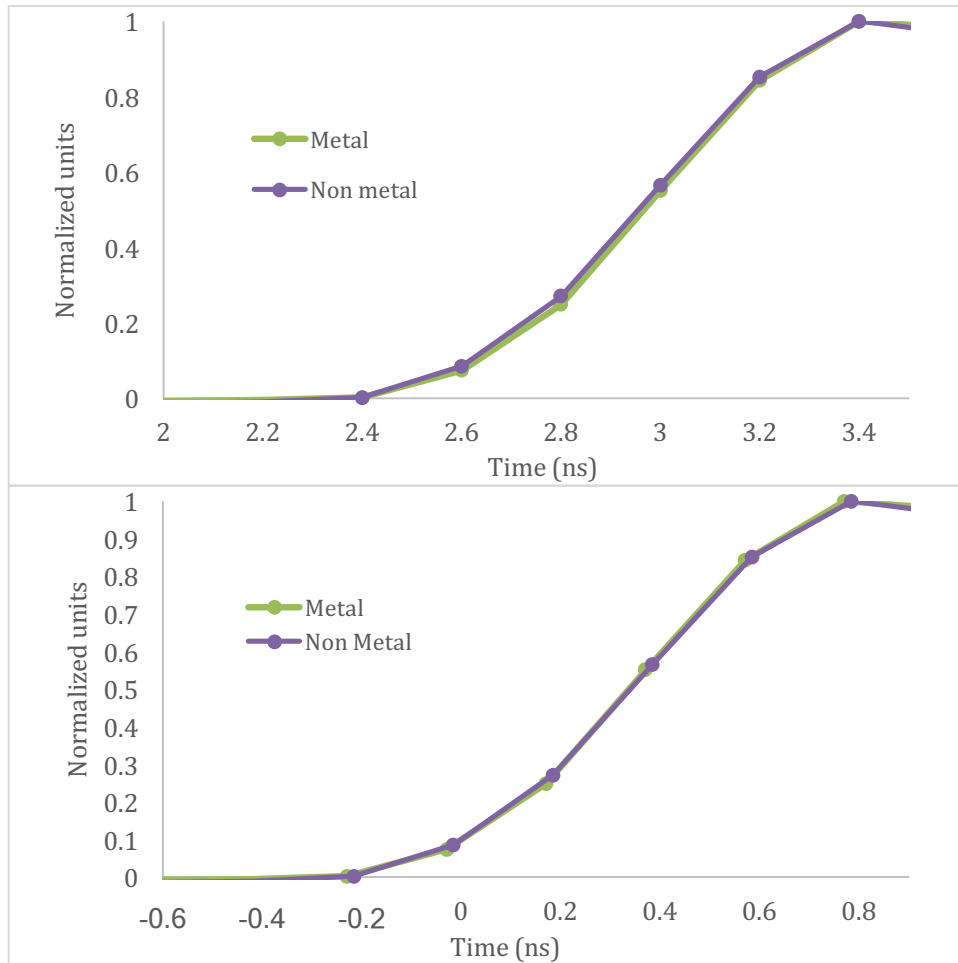
Figure 30. Average pulses, W11LGA35. Pulses are normalized. (top) Uncorrected (bottom) aligned at 10% of the pulse height. It appears that the pulses in the metalized region have slightly faster rise times, though they arrive later prior to correction.

### 3.1.4 CFD scans

To optimize timing results we calculated time resolutions for varying CFD%s on the DUT, shown in Figure 31. In previous results with the fast scope [9], we the optimal time resolution was with a CFD% near 15%, but here the minimum time resolutions occur at CFD%>60%.

40
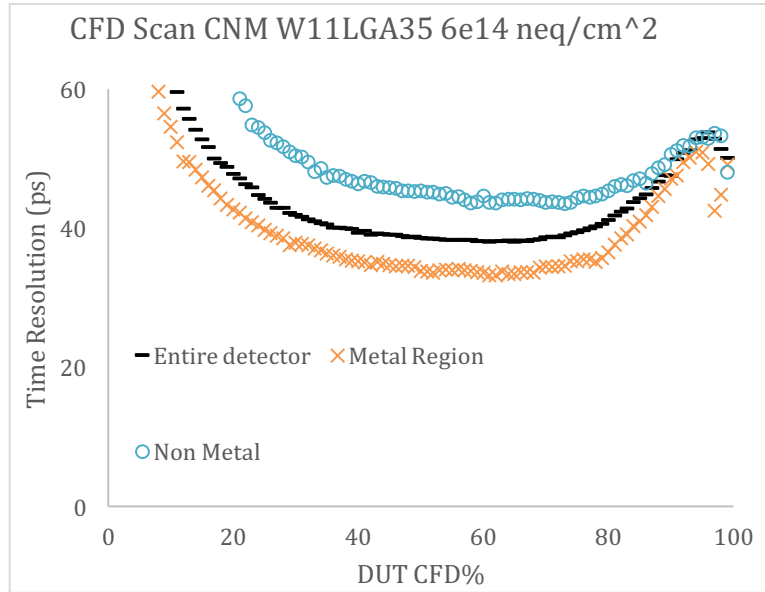
Figure 31. Time resolution versus CFD%, various regions as a function of various CFD% on the DUT and trigger. Time resolutions for the metallized region, non-metallized, and entire sensor are plotted here. The metallized region of the sensor has a smaller time resolution at most of the CFD%s, with the exception of a few of the higher and lower percentages.

Table 3. Minimum time resolution values and corresponding CFD%s of CNM W11LGA35 for the interior non-metallized region, the exterior, metalized region, and the entire diode.

| Region | Time Resolution (ps) | DUT CFD% at Minimum |
|---|---|---|
| Entire Sensor | 38.0±0.5 | 61 |
| Metal | 33.2±0.9 | 62 |
| Non-metal | 43.5±0.9 | 73 |

In correspondence with the lower pulse height measured in the central region of the sensor, we calculated consistently greater time resolutions for the non-metallized region.

This timing analysis will also be discussed in Chapter 4 in which we compare results for two different digitization systems.

3.2 HPK array, 50C PIX, non-irradiated

As can be seen in Figure 6, only the center of HPK arrays were covered in metal, whereas the perimeter region is exposed silicon oxide. The square central region is covered by grey-colored metal of dimensions 1.5mm by 1.5mm, effectively covering one quarter of the total sensor area. Based on the drastic differences in pulse height and gain and smaller differences in timing for the metallized and non-metallized regions of the irradiated CNM diode, we investigated potential effects of the metal in HPK sensors. In particular, we studied the timing, gain, and pulse height of different regions of the sensor.

We analyzed the same data from the HPK 50C PIX sensor mounted on a UCSC four channel board as in Chapter 2 on the measurement of the width of inactive regions. For the studies on gain and pulse maximum, we wanted to see if the non-irradiated HPK array would have higher pulse heights in regions with metallization on top, as the CNM irradiated diode exhibited. For the gain and pulse height analysis, we used data acquired with multiple bias voltages for the sake of increased statistics, as in Chapter 2. With only events from a single bias setting, many bins in the plots below would become sparsely populated. For timing studies, we selected a single bias voltage of -450V.

3.2.1 Timing studies

With the same methodology for defining events as in Chapter 2, we measured the timing resolution and mean time difference of the sensor as a function of each planar spatial dimension. We used a CFD% of 50% for both the DUT and trigger.

42

Due to poor statistics, only channels 1 (blue) and 4 (black) were used to make the

timing resolution profile. The results are shown in Figure 32 and Figure 33 and are

relatively uniform. For CNM we measured a gain of 10 at -180V bias and for HPK a

gain of 24 at -450V bias.



Figure 32. Timing resolution profiles of HPK 50C PIXbiased at -450V. Only 2 channels are plotted; channels 1 is in blue and channel 4 in black. Bins are 300μm wide.
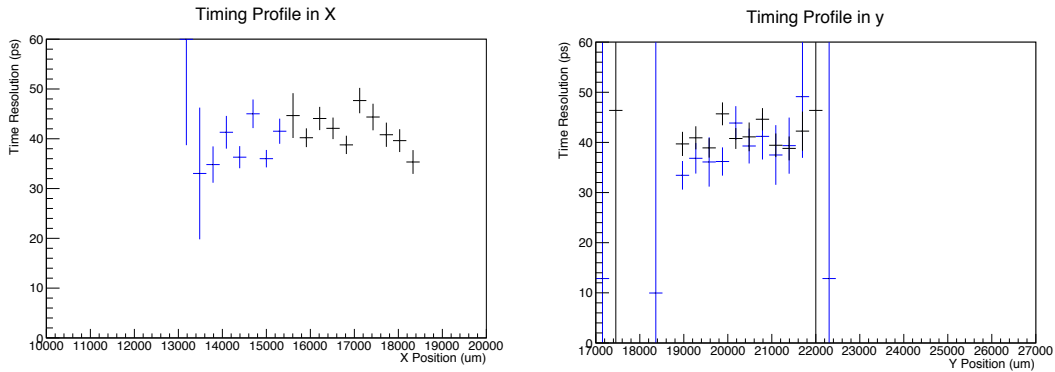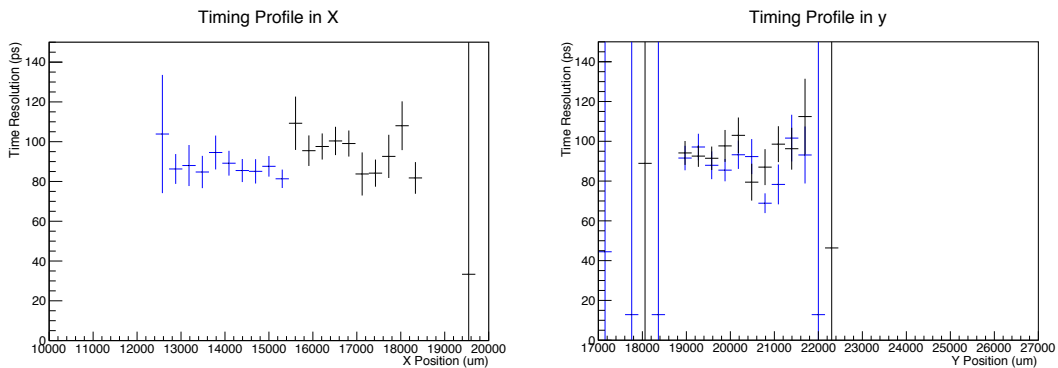


Figure 33. Timing resolution profiles of CNM W9HG11 biased at 180V. Only 2 channels are plotted; channels 1 is in blue and channel 4 in black. Bins are 300μm wide.

As can be seen in Figure 34, signals from the four pixels had significantly

different mean time differences, presumably due to signal path length differences. We

will show it is in fact due to the differences in length of the traces on the UCSC 4-channel board. Error bars correspond to the error on the mean of the Gaussian fit to the time differences, with large error bars due to low statistics. Note that the points in green corresponding to the upper left pad have especially erratic behavior. This is due to the limited number of events that hit this part of the array, as is apparent Figure 17, Figure 18, and Figure 19. Also note that we have plotted a few missed tracks.

Due to these differences in the mean times, for the purposes of timing studies channels had to be analyzed separately. Assuming the signal propagates at half the speed of light, as is approximately the case for PCB traces, we may approximate that the ~500ps difference implies the length difference to be close to 7cm.
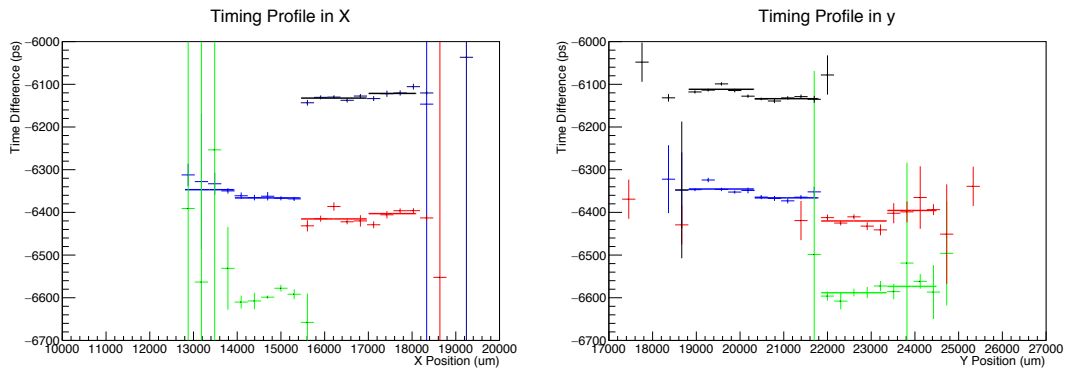


Figure 34. Profiles of the of mean time difference for HPK 50C PIX biased at -450V. The different colors correspond to different pixels on the sensor, with the color coordination matching Figure 17. Fits are to a constant value. Fits to channel 2 in the x-direction are omitted due to poor statistics, which are reflected its large error bars. Bins are 300μm wide.

Furthermore, Figure 34 shows that for individual channels, the mean time difference becomes smaller by 10-20ps near the center of the sensor where there is metal. The time differences are fit with a constant value for the metallized and non-

metallized regions, and in each case the metallized region has pulses which arrive sooner. In the time difference profiles of the CNM array W9HG11 biased at -180V in Figure 35, there is not the same pattern of earlier pulses near the center, suggesting the difference is due to the sensors and not a consistent feature. The relative times of the pixels also match the pattern for the HPK array in Figure 35, suggesting that the origin of the large-scale differences between channels is unlikely due to differences in cable length, but due to the readout, the UCSC four channel boards, or the data acquisition system, the CAEN V1742.
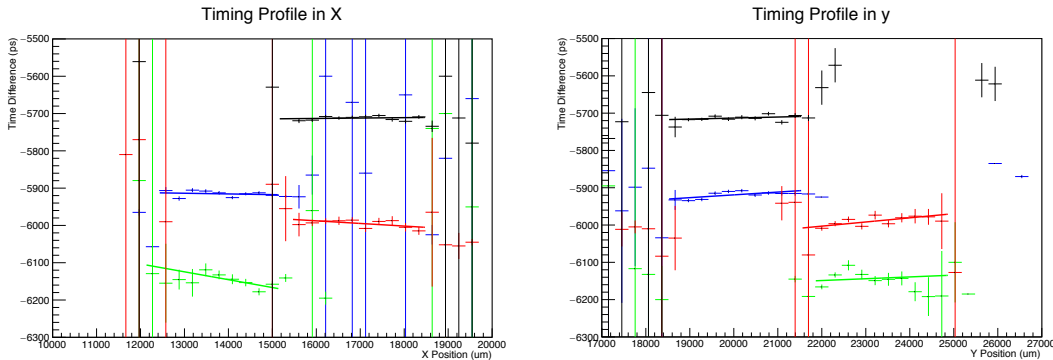


Figure 35. Profiles of the of mean time difference for CNM W9HG11 biased at -180V. Results from each pixel are fit with a 1$^{st}$ degree polynomial. Bins are $300\mu m$ wide.

By measuring the traces on the UCSC four channel board and assuming signals to propagate at half the speed of light, we can approximate the expected delay between channels. The results of this calculation are show in Table 4, and match the results in Figure 34 and Figure 35. We are thus confident this difference in mean time is due to path length differences on the board, and are not an intrinsic feature of the sensor.

Table 4. Length of traces and corresponding signal times for the UCSC 4-channel board. The times have been shifted by 5700ps to match those in Figure 34 and Figure 35.

| Channel | Length of trace (inches) | Adjusted time of signal (ps) |
|---|---|---|
| 0 (blue) | 2.701 | -5977.666667 |
| 1 (green) | 1.79 | -6129.5 |
| 2 (red) | 2.625 | -5990.333333 |
| 3 (black) | 4.367 | -5700 |

3.2.2 Average pulse shapes

To investigate the cause of the earlier pulses on the metallized region, we compared the leading edges of average pulse shapes from the metallized and non-metallized regions of the HPK array. Presumably, the earlier pulses may be due to a change in pulse shape such as a faster rise time, as opposed to simply being translated by a small duration.
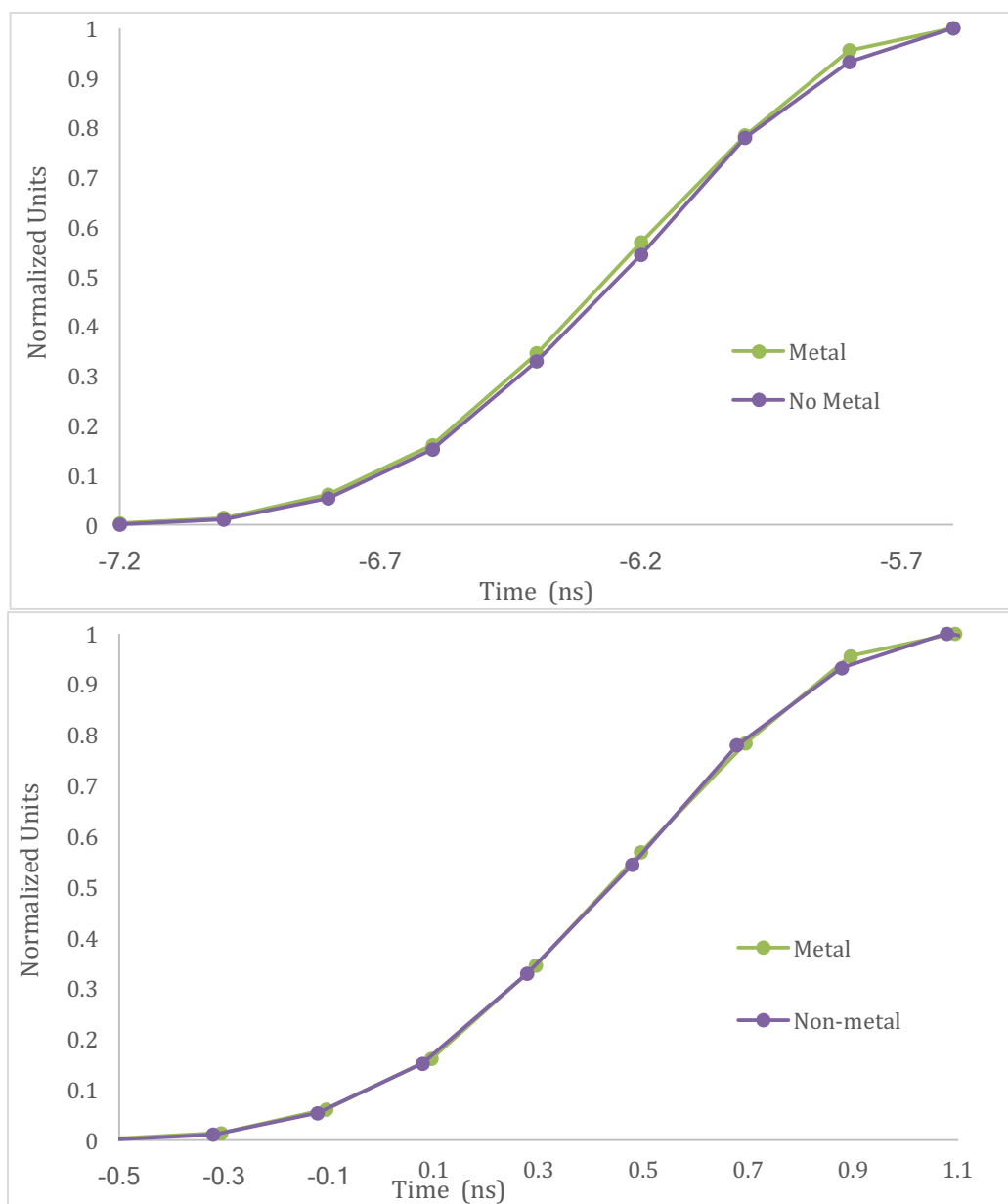
Figure 36. Average pulse shapes of HPK 50C PIX for the metallized (purple) and non-metallized (green) regions. In (bottom) the pulses have been corrected relative to each other such that they cross t=0 at 10% of the pulse height. There is no correction in (top), and the delay between the two pulses at 50% is 20ps, matching the results in Figure 34.

In Figure 36, we can notice a small difference in the pulse shapes: when they are aligned at 10% of the pulse height in Figure 36 (bottom), the pulse on the metal reaches its maximum slightly later, but 90% of its pulse height slightly earlier; the

rise time on the metal is 20ps faster for these average pulses. Hence, it would seem the earlier timing is due to a change in the rise time and pulse shape, however, we hesitate to make this conclusion based the small size of this difference. The pulses are too similar. Also, the results from the CNM diode indicate that pulses from the metallized regions may have faster rise times, but arrive later as opposed to earlier.

3.2.3 Pulse Maximum Profiles

As previously described, we measured the gain of the sensor to create 2-dimensional gain profiles. Here, we expected that there may be greater gain height in the metallized region, since this was measured in the CNM irradiated diode.
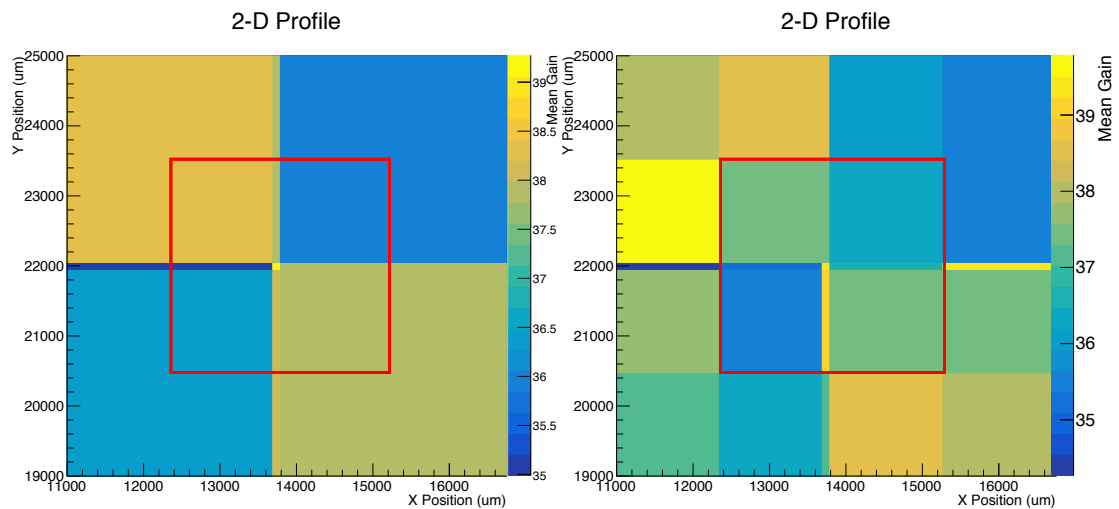


Figure 37. Gain profiles of HPK 50C PIX at multiple bias voltages. The region inside the red square corresponds to the region which has metal on the surface. Bins are 3mm square in (top left) 1.5mm in (top right), and .75mm in (bottom).

2-D Profile
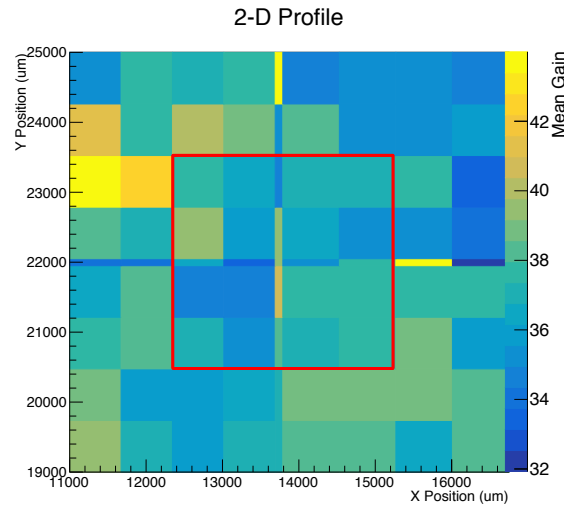
Figure 37 (bottom)

In Figure 37, there is not a significant difference in the gain between the two regions. The slightly erratic measurements in the upper left pad can be attributed to the low statistics in that region. The only pixel which has a higher pulse height in the metallized region is the upper right.

Chapter 4: Comparison of Digitizers

4.1 Introduction

An important parameter for the development of fast particle detection are the bandwidth requirements of the digital readout system. In the the FNAL test beam, we used a CAEN V1742 digitizer board with a bandwidth of 500MHz and sampling rate of 5GS/s for the data acquisition. At SCIPP in [9, 17], we measured the timing resolution of the same irradiated diode sensors in a $^{90}$Sr beta beam and used a Teledyne Lecroy WavePro725Zi oscilloscope with a 2.5GHz bandwidth and sampling rate of 40 GS/s. In this section, we compare the results for the two data acquisition systems, with the caveat that we also have different trigger detectors and particle types which are supposed to behave as MIPs in these two cases: 2 MeV electrons for the beta source, and 120GeV pions at the FNAL test beam.

In UFSD, we have modeled the time resolution as the square of sum in quadrature of a number of contributing factors [17]:

$$\sigma_t^2 = \sigma_{jitter}^2 + \sigma_{time\ walk}^2 + \sigma_{Landau}^2 + \sigma_{distortion}^2 + \sigma_{TDC}^2$$

In particular, $\sigma_{TDC}$ is the timing uncertainty due to the sample rate of the time-to-digital converter, modeled as

$$\sigma_{TDC} = \frac{bin\ size}{\sqrt{12}}$$

for a simple threshold trigger. For the CAEN V1742, the 200ps bins imply $\sigma_{TDC} = 57.7$ps, suggesting that we would not be able to replicate results in beta testing where we measured irradiated LGADs to have time resolutions near 30ps. However, for an

interpolated trigger, as we use in the CFD method, the timing error may be significantly less. Specifically, for the error on the voltage due to interpolation, $R$,

$$R < \frac{t_1 - t_0}{8} \max_{t_0 < t < t_1} |f''(t)|$$

where $f(t)$ is a function that describes the voltage of a pulse at a given time, $t_1$ and $t_0$ are the digital times between which the interpolation occurs, and thus $t_1 - t_0$ is again the bin size [19]. Though $f$ is unknown, this formula implies that it may be possible to achieve better timing. In an ideal example, if the pulse is linear in the region of interpolation, $R$, and then also the uncertainty in time, equal 0. A real pulse will be unlikely to be perfectly linear, but by using interpolation, $\sigma_{TDC}$ may be improved.

Another important term is the jitter, $\sigma_{jitter}^2$, the uncertainty in timing due to the slew rate (dV/dt) and variance in voltage. We calculate the jitter as

$$\sigma_{jitter} = \frac{Rise\ Time}{(Signal - to - noise)}$$

where the signal to noise is the pulse height divided by the noise RMS. A detector's time resolution should also be limited by the jitter. We measure larger jitter values in test beam results than beta results, though essentially the same time resolutions, suggesting that jitter is not the main contributor to the time resolution.

Time walk, $\sigma_{time\ walk}^2$, is variance in timing that arises when using a fixed threshold to timestamp events. Essentially, pulses with the same rise time but different pulse heights will have different timestamps at the same threshold. By using a CFD algorithm, we can eliminate this contribution to the time resolution.

The timing variance due to distortion of the electric field, $\sigma^2_{distortion}$, is also only a minor contributor to the overall resolution. The electric field is uniform near the center of the detector, with variations near the edges of detectors. Hence, particles which pass near the edge may induce a different sized or shaped signal. However, since the detector thickness to width ratio is small, this effect should be a minimal contribution to the time resolution.

The Landau noise, $\sigma^2_{Landau}$, is then presumably a significant contributor to the time resolution. This arises from variations in the pulse shape due to non-uniform local energy dissipation as ionizing radiation passes through the detector.

4.2 Gain and timing of diodes at FNAL

As discussed in Chapter 3, we analyzed the timing capabilities of W11LGA35 6e14neq/cm$^2$. In this chapter, we reference these results and also show timing analysis of HPK 50D 6e14neq/cm$^2$. We also calculate the gain, which has been strongly correlated with the timing resolution of UFSDs.

In Figure 38 we show the gain distributions of the two irradiated diodes. The gain calculation is based on the single channel board transimpedance, secondary amplifier gain, and the predicted charge deposited by a MIP as a function of detector fluence. Values are comparable to beta testing results, which are summarized in Table 6. Other results in this table, such as the rise time and pulse amplitude, are calculated by fitting distributions of the given parameter. For pulse maximum and gain, we use a Landau fit, whereas for other measurements we use Gaussian fits. In (right) of Figure 38, the distributions for different regions of the sensor are plotted, with most probable

gain values of 9.3, 18.1, and 14.4 for the inside, outside, and the entire sensor,

respectively. For the sake of comparison to beta injection results, the gain of the

entire sensor is used.

In Figure 39 and Figure 40, we show the CFD scans for the CNM and HPK

diodes. As with the CNM diode, we achieve a minimum time resolution near 40ps, as

tabulate in 4.1. Furthermore, we note that the CFD% at which the minima of the time

resolution occur are tend to be lower (<18%) for the fast scope data, than for the

CAEN V1742 data (>66%).
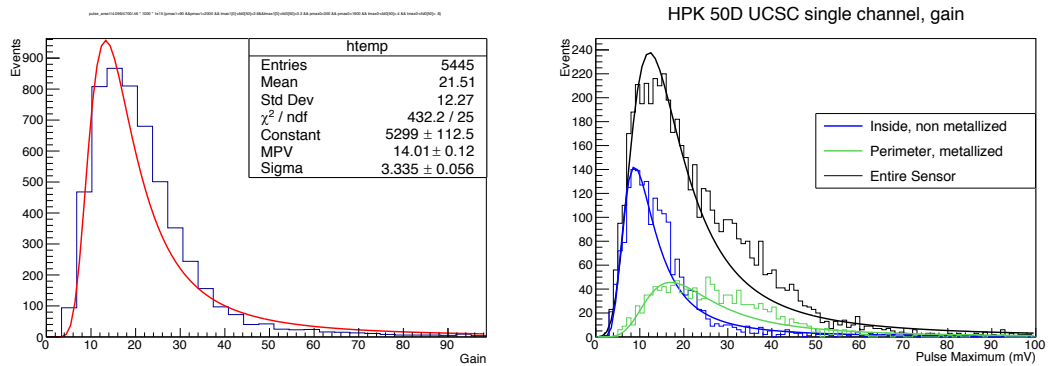


Figure 38. Distribution of gain values of the irradiated diodes of fluence
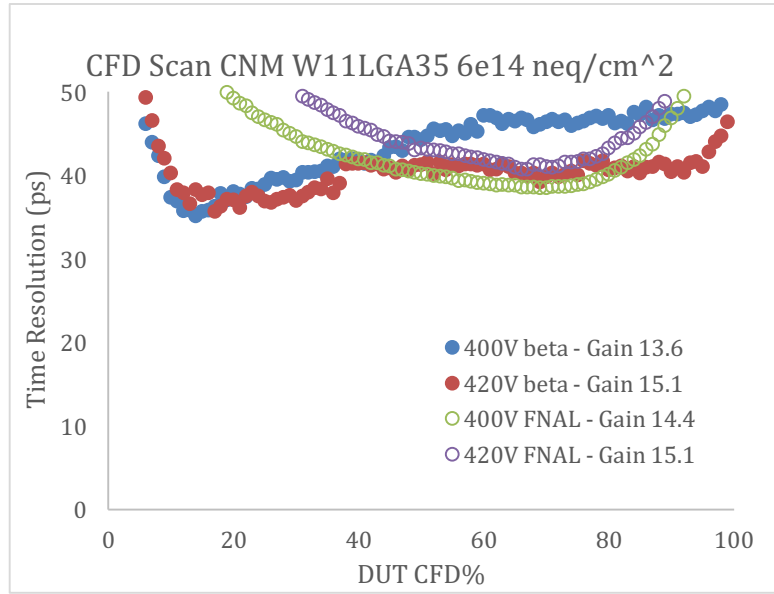6e14neq/cm$^2$: (left) HPK 50D and (right) CNM W11LGA35.

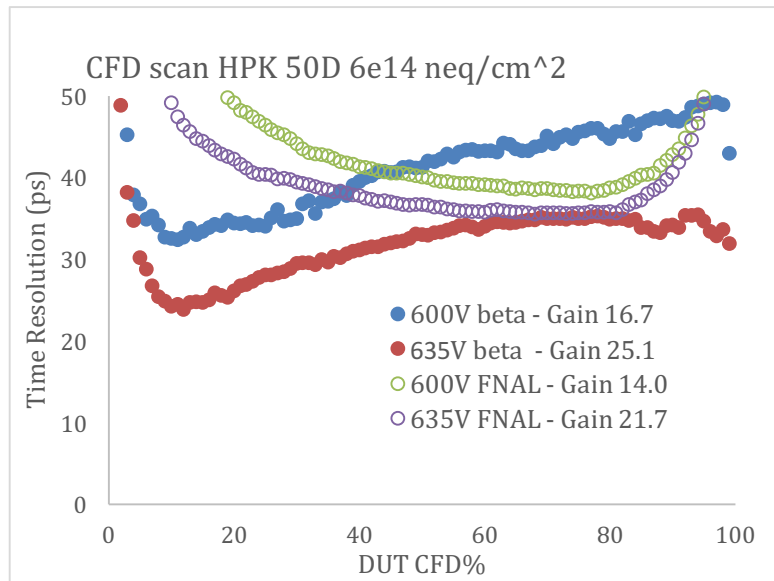Figure 39. CFD scan for CNM W11LGA35 6e14 neq/cm$^2$. Trigger CFD% is 20%.



Figure 40. CFD scan for HPK 50D 6e14 neq/cm$^2$. Trigger CFD% is 20%.

Table 5. Minimum timing resolutions for single diodes tested at FNAL and in beta testing at UCSC.

| Sensor | Bias (V) | Time Res (ps) [FNAL ] | DUT CFD% at Min [FNAL] | Time Res (ps) [beta] | DUT CFD% at Min [beta] |
|---|---|---|---|---|---|
| CNM W11LGA 6e14 neq/cm$^2$ | 400 | 38.5 ±0.5 | 69 | 35.1±1.3 | 14 |
| | 420 | 40.7 ± 0.6 | 67 | 35.7±1.6 | 17 |
| HPK 50D 6e14 neq/cm$^2$ | 600 | 38.2± 0.4 | 77 | 32.5±1.4 | 12 |
| | 635 | 35.5±0.5 | 68 | 22.6±1.1 | 12 |

4.3 Average pulses, other measurement

Methodology for the beta injection measurements at UCSC are described in [16, 17] and analysis methods are virtually identical to those used in this thesis. In Figure 41, we compare the average pulses from the beta injection and test beam. As we expect at a lower bandwidth, the pulses from the test beam have lower amplitudes and longer rise times, suggesting that their timing may be worse. However, we expected and measured a lower noise RMS in the FNAL data, which should improve timing.

The results extracted from fits are tabulated in Table 6. Though the noise is lower for the CAEN V1742, the lower signal and slower rise time result in a greater value for the jitter. This would seem to suggest that we would find inferior timing results for the FNAL data. This is not the case, as shown in Table 6. The measured gain values at FNAL were greater for the CNM sensors by ~5%, and smaller for the
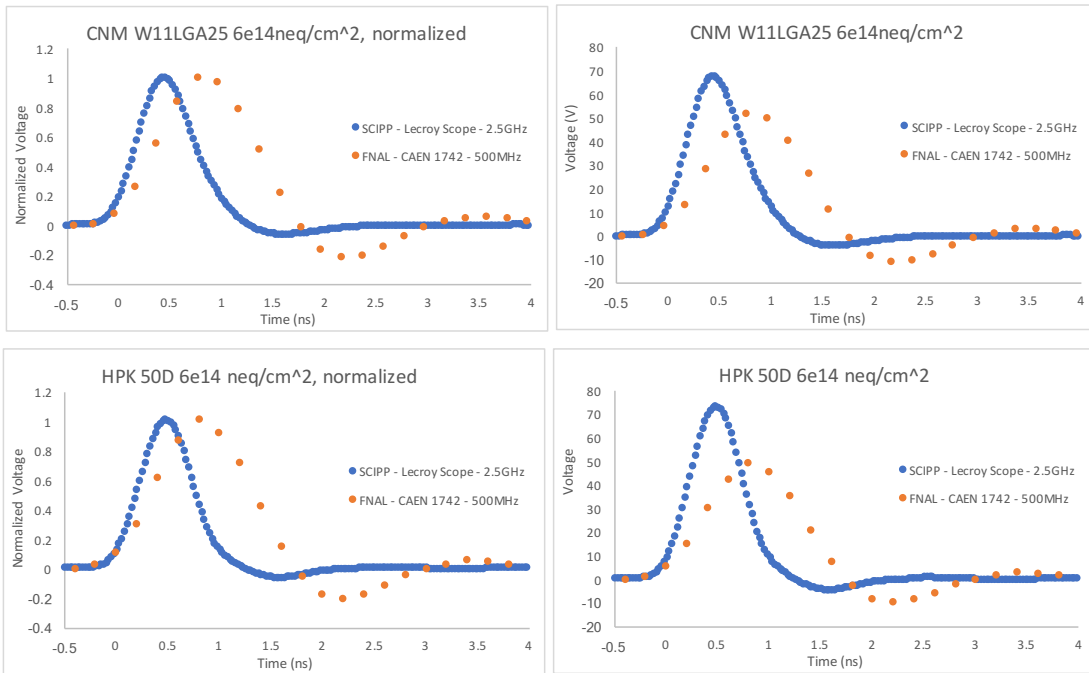
HPK sensors by ~20%.



Figure 41. Average pulse shapes for irradiated diodes in the test beam and beta source. For CNM, data with 400V bias is selected, for HPK it is data at 600V bias.

Table 6. UFSD parameters for irradiated diodes in test beam and beta source. Uncertainties are the error values from fits. All sensors were tested at -20° C.

| Sensor | Lab/Bandwidth | Bias (V) | Gain | Pmax (mV) | Noise RMS (mV) | Rise time (ps) | Jitter (ps) | Time Res (ps) |
|---|---|---|---|---|---|---|---|---|
| HPK | UCSC/2.5GHz | 600 | 16.7±.2 | 59.3±0.7 | 1.8±0.0 | 373.7±1.6 | 12 | 32.5±1.2 |
| | FNAL/.5GHz | 600 | 14.0±.1 | 34.2±0.2 | 1.3±0.0 | 645.0±0.8 | 24.3 | 38.2± 0.4 |
| | UCSC/2.5GHz | 635 | 25.1 ±0.2 | 91.2±0.9 | 1.8 ± 0.0 | 388.6±0.8 | 7.5 | 22.6±1.1 |
| | FNAL/.5GHz | 635 | 21.7±.2 | 52.1±2.7 | 1.3±0.0 | 636±0.7 | 15.7 27.9 | 35.5±0.5 |
| CNM | UCSC/2.5GHz | 400 | 13.6±.2 | 45.0±1.4 | 1.9±0.0 | 377.5±1.5 | 20 | 38.5 ±0.5 |
| | FNAL/.5GHz | 400 | 14.4±.2 | 29.9±0.7 | 1.3±0.0 | 641.0±0.8 | 27.9 | 35.5±1.3 |
| | UCSC/2.5GHz | 420 | 15.1±.2 | 48.6±1.1 | 2.8±.2 | 367.8±1.7 | 21.4 | 40.7 ±0.6 |
| | FNAL/.5GHz | 420 | 15.7±.2 | 34.4±0.5 | 1.3±0.0 | 631.0±1.1 | 23.9 | 37.5± 0.9 |

The results in Table 6 show that timing results on the order of 35ps can be achieved with a lower sampling rate and bandwidth digitizer. Apparently, by using a CFD algorithm and interpolating, we vastly improve the on the 57ps of uncertainty predicted for a threshold algorithm and TDC with 200ps bins. In future experiments, it will be interesting to try different configurations to further test the relationship between digitizer specifications and measured time resolutions of sensors. Ideally, we would send even faster sensors that have not been irradiated to a test beam where we would implement multiple data acquisitions system with varying bandwidth and sampling rates.

Chapter 5: Conclusions

We can draw a number of conclusions from our analysis of LGADs at the May 2017 FNAL test beam:

For the arrays, we measured the width of the inactive regions in CNM and HPK pixel arrays to be 71μm and 111μm, respectively. The area of the active regions is 3mm by 3mm, as designed.

For the irradiated single diodes, the CNM diodes have active and gain regions approximately matching that of GDSII masks. The HPK diode's gain region is a circle of radius 1mm. Pulses from the metallized region in the CNM sensor have greater gain, better timing resolution, and there is an indication of slightly faster rise times. However, the time differences are on average later for the metallized region, suggesting there may be more happening than the change in rise time.

In the unirradiated HPK array, the gain and time resolution were measured to be uniform across the sensor. In particular, they were the same in metallized and non-metallized regions, suggesting that the effect of metallization depends on irradiation. Pulses from the metallized region arrive earlier in this sensor, the opposite of what occurred in the CNM irradiated diode. There is an indication of slightly faster rise times (~20ps, or ~5%) for pulses in the metallized region, which may cause the early pulses.

We do not propose a mechanism to explain the behavior of signals in metallized and non-metallized regions. The measureable effects on gain and time resolution only occur in the irradiated sample, though in both sensors, there is a small

(10-20ps) shift in the mean time of arrival for metallized regions. It may be of interest to test irradiated HPK diodes with the same geometry for metallization, and study unirradiated sensors with more statistics, for which beam alignment is crucial.

Timing and gain results using the CAEN digitizer at FNAL are comparable to results from beta testing with the Teledyne Lecroy 2.5GHz oscilloscope for readout. For single diodes from CNM and HPK irradiated at 6e14neq/cm$^2$, we measure time resolutions near 35ps and comparable gain values. Further studies comparing the results of digitizers, in particular with faster sensors, may be prudent.

# References

[1]   F. Hartmann, Evolution of Silicon Sensor Technology, Springer-Verlag Berlin Heidelberg, 2009.

[2]   H. F.-W. Sadrozinski, A. Seiden, N. Cartiglia, 4-Dimensional Tracking with Ultra-Fast Silicon Detectors, arXiv:1704.08666 [physics]

[3]   The ATLAS Collaboration. (2015). Phase II Upgrade Scoping Document [Online] Available: http://cds.cern.ch/record/2055248/files/LHCC-G-166.pdf?version=2

[4]   I. Tapan et al., Avalanche photodiodes as proportional particle detectors, Nuclear Instruments and Methods in Physics Research Section A 388 (1997) 79.

[5]   G. Pellegrini et al., Technology developments and first measurements of Low Gain Avalanche Detectors (LGAD) for high energy physics applications, Nuclear Instruments and Methods in Physics Research, Section A 765 (2014) 12.

[6]   W. Maes, K. De Meyer, R. Van Overstraeten, Impact ionization in silicon, a review and update, Solid-State Electronics 33 (6) (1990) 705.

[7]   A. Macchiolo, Impact ionization in silicon detectors, in: Sixteenth RD50 Workshop Barcelona, Spain, 2010, ⟨https://indico.cern.ch/event/86625/contributions/2103500/attachments/1080657/1541404/Simulation.pdf⟩.

[8] N. Cartiglia, Ultra Fast Silicon Detectors, CERN Detector Seminar, 86 Geneva, Switzerland, 26 September, 2014, https://indico.cern.ch/event/329886/attachments/641603/882830/CERN UFSD Cartiglia.pdf.

[9] H. F.-W. Sadrozinski et al., Properties of HPK UFSD after neutron irradiation up to 6e15 n / cm 2, arXiv: 1707.04961 [physics]

[10] S. Kwan et al, The pixel tracking telescope at the Fermilab Test Beam Facility, Nuclear Instruments and Methods in Physics Research Section A 811 (2016) 162.

[11] Z. Luce, UCSC Senior Theses 2017, https://drive.google.com/drive/folders/0ByskYealR9x7bFY1ZS1pZW9SRWs..

[12] M. Carulla e. al., First 50 m thick LGAD fabrication at CNM, in 28th RD50 Workshop, Torino, 2016. https://agenda.infn.it/getFile.py/access?contribId=20&sessionId=8&resId=0&materialId=slides&confId=11109

[13] A. Ronzhin et al., Study of the timing performance of micro-channel plate photomultiplier for use as an active layer in a shower maximum detector, Nuclear Instruments and Methods in Physics Research Section A  795 (2015) 288.

[14] A. Apreysan et al., Test Beam Studies Of 50 μm LGAD sensors, unpublished

[15] A. Ronzhin et al., A new time calibration method for switched-capacitor-array-

based waveform samplers, Nuclear Instruments and Methods in Physics

Research Section A  767 (2014) 67.

[16]  C. Labitan, UCSC Senior Thesis 2017,

https://drive.google.com/drive/folders/0ByskYealR9x7bFY1ZS1pZW9SRWs.

[17]  Y Zhao, UCSC Senior Thesis 2017,

https://drive.google.com/drive/folders/0ByskYealR9x7bFY1ZS1pZW9SRWs.

[18]  S. Meroli et al, Energy loss measurement for charged particles in very thin

silicon layers, JINST 6 (2011) P06013.

[19]  H. Grabas, Development of a measurement system of picosecond time in the

ATLAS experiment, l'Université Paris Sud Dissertation